TECHNISCHE UNIVERSITÄT WIEN
Vienna | Austria

Master Thesis

Experimental Investigation on Partial Cycle Operation of High Temperature Latent Heat Thermal Energy Storage Systems

carried out for the purpose of obtaining the degree of Master of Science (MSc or Dipl.-Ing. or DI), submitted at TU Wien, Faculty of Mechanical and Industrial Engineering, by

Paul Schwarzmayr
Matr.Nr.: 01527078

under the supervision of
Ao. Univ.Prof. Dipl.-Ing. Dr.techn. Heimo Walter
Institute for Energy Systems and Thermodynamics, E302

and
Dipl.-Ing. Dr.techn. Georg Scharinger-Urschitz
Institute for Energy Systems and Thermodynamics, E302

Vienna, December 2020

Author
Paul Schwarzmayr
Matr. Nr.: 01527078
paul.schwarzmayr@tuwien.ac.at

Supervisor
Ao. Univ.Prof. Dipl.-Ing. Dr.techn. Heimo Walter
TU Wien
Institute for Energy Systems and Thermodynamics
Getreidemarkt 9, A-1060 Wien

Supervisor
Dipl.-Ing. Dr.techn. Georg Scharinger-Urschitz
TU Wien
Institute for Energy Systems and Thermodynamics
Getreidemarkt 9, A-1060 Wien

Affidavit
I declare in lieu of oath, that I wrote this thesis and performed the associated research myself, using only literature cited in this volume. If text passages from sources are used literally, they are marked as such. I confirm that this work is original and has not been submitted elsewhere for any examination, nor is it currently under consideration for a thesis elsewhere.

Vienna, December, 2020

Paul Schwarzmayr

Abstract

This thesis examines a high temperature latent heat thermal energy storage system at partial cycle operating conditions. A storage system of this type could find use in modern concentrated solar power- and combined heat and power plants. In contrast to lab-scale experiments, which only operate at full charging/discharging cycles, utility-scale storage systems will also have to deal with partial charging/discharging cycles. Therefore the behaviour of a latent heat thermal energy storage at partial cycle operating conditions is the focus of this thesis.

The examined test rig consists of a single shell-and-tube heat exchanger with a storage capacity of 7.91 kW h. The heat exchanger surface is equipped with a combination of arborescent longitudinal and transversal aluminium fins for heat transfer enhancement. Sodium nitrate, with a melting temperature of 306 °C, is utilized as phase change material and a thermal oil plant provides the storage system with 280 kW_{th} of heating- and 205 kW_{th} of cooling power.

For the characterization of the storage, a formulation for the state of charge which is based on a distribution function of the enthalpy of fusion is developed. Power rates are calculated from the measured data and plotted against the state of charge in order to make a statement of the partial cycling behaviour of the examined thermal energy storage. For validation of the measured data and accuracy assessment of the state of charge formulation, the energy balance for the storage tank is calculated.

The data analysis shows promising results like constant power rates for every state of charge and all the examined partial cycle operation modes. The mean power rates for charging and discharging are 6.78 kW and −5.62 kW respectively. The 95.45 % confidence interval is ±1.14 kW for charging and ±1.36 kW for discharging. At this point it should be emphasized that the innovation of this work is not the measured power rate, but rather the low confidence intervals. The lowest power rate is measured for the full cycle at the end of charging/discharging. It is caused by a narrow volume, which is not penetrated by fins, near the perimeter of the cylindrical heat exchanger. The energy balance shows that the developed state of charge formulation very well correlates with the measured data for a charging process. For a discharging process, the state of charge formulation shows a significant deviation from the measured data which has to be carefully taken into account when considering the results. The energy density is as high as 110 kW h m^{-3} and a mean discharging power rate of 2.28 kW m^{-1} for the finned tube is confirmed. These values are highly promising for further development and application of latent heat thermal energy storage systems.

Kurzfassung

In dieser Arbeit wird das Be- und Entladeverhalten eines Hochtemperaturlatentwärmespeichers ausgehend von teilbe- oder entladenen Speicherzuständen untersucht. Solch ein Speichertyp kann beispielsweise in modernen thermischen Solarkraftwerken oder Kraftwerken zur Kraft-Wärme Kopplung zum Einsatz kommen. Im Unterschied zu Experimenten im Labormaßstab wird sich ein thermischer Speicher in einem thermischen Solarkraftwerk zum Großteil der Zeit in einem teilbe- oder entladenen Zustand befinden. Der Schwerpunkt dieser Arbeit ist daher die Untersuchung des Betriebsverhaltens eines Latentwärmespeichers ausgehend von teilbe- bzw. entladenen Zuständen.

Der Versuchsaufbau besteht aus einem Doppelrohrwärmetauscher mit einer maximalen Speicherkapazität von 7.91 kW h. Zur Verbesserung des Wärmeübergangs wird eine Kombination aus Längs- und Querrippen, welche aus Aluminium gefertigt werden, verwendet. Als Phasenwechselmaterial wird Natriumnitrat, welches einen Schmelzpunkt von 306 °C aufweist, verwendet. Durch eine Thermoölanlage wird der Versuchsaufbau mit einer maximalen Heizleistung von 280 kW_{th} und einer maximalen Kühlleistung von 205 kW_{th} versorgt.

Für die Bestimmung des Ladezustandes des Speichers wird, basierend auf einer Verteilungsfunktion für die Schmelzenthalpie, eine mathematische Formulierung für den Ladegrad (englisch: state of charge) entwickelt. Um das Betriebsverhalten des untersuchten Latentwärmespeichers zu bewerten, wird aus den gemessenen Daten die Leistung des Speichers berechnet und in Abhängigkeit des Ladegrades graphisch dargestellt. Weiters wird eine Energiebilanz für den Speicher aufgestellt, um damit die Messwerte zu validieren und um eine Aussage über die Anwendbarkeit der entwickelten Ladegradformulierung für die Charakterisierung eines Latentwärmespeichers machen zu können.

Die Ergebnisse der Datenauswertung sind sehr vielversprechend. Die mittlere Leistung beträgt 6.78 kW (95.45 % Konfidenzintervall=±1.14 kW) für den Ladeprozess und -5.62 kW (95.45 % Konfidenzintervall=±1.36 kW) für den Entladeprozess. An dieser Stelle sollte man herausheben, dass die Innovation dieser Arbeit nicht die gemessenen Leistungen, sondern viel mehr die kleinen Konfidenzintervalle sind. Die geringste Leistung wird für den vollen Zyklus am Ende des Be-/Entladeprozesses gemessen. Grund dafür ist, dass sich in den äußersten Bereichen des Speichers keine Aluminiumrippen mehr befinden, was sich negativ auf den Wärmetransport in diesem Bereich auswirkt. Aus der Energiebilanz geht hervor, dass sich die entwickelte Ladegradformulierung sehr gut für die Beschreibung eines Ladeprozesse eignet, jedoch nicht für die eines Entladeprozesses. Die Energiedichte für den untersuchten Speicher beträgt 110 $kW\,h\,m^{-3}$ und die mittlere Ladeleistung für die Rippenrohre ist mit 2.28 $kW\,m^{-1}$ gegeben. Diese Ergebnisse sind sehr vielversprechend für die weitere Entwicklung und Anwendung von Latentwärmespeichern im industriellen Maßstab.

Acknowledgments

This thesis, the final part of my master's degree, wouldn't have turned out so well (at least I believe it has turned out well) if it weren't for some important people.

First and foremost, I want to acknowledge my supervisors Heimo Walter and Georg Scharinger-Urschitz. They guided me into the world of scientific research and supported me and my work during the last couple of month. Thank you for the trust you placed in me when you invited me to take part in the publication of the journal paper [53] on which this thesis is based.

Further, I want to thank the head of the IET, Markus Haider, who facilitated my work at the IET as a teaching assistant during the last two years. This employment gave me the opportunity to learn a lot about teaching and to daily communicate with professors and PhD students at the IET which significantly increased my knowledge on thermal engineering and scientific working.

It gives me great pleasure to thank Karl Ponweiser and Heimo Walter for the appreciative collaboration over the past two years which, for me, has been enriching in every sense. From you, I learned a whole lot about the fundamentals of thermodynamics and their applications. Thanks for always taking time on any of my questions, no matter how long it took for me to understand your explanations.

I am also very proud to mention my amazing colleagues at the IET who accompanied me for the last two years. Thank you David, Georg, Stefan, Rouzbeh, Verena and Viktoria for your companionship. Spezial thanks to Felix who always supported me with his expertise and helped me to improve the quality of this thesis.

Just as importantly, I want to thank my family, friends and fellow students who accompanied and supported me on this journey, be it on a mental or technical level. A special thank you goes to my brother Florian who proofread this thesis.

Contents

Nomenclature

Acronyms

CAES	compressed air energy storage
CHP	combined heat and power
DLR	German Aerospace Center
DNV GL	Det Norske Veritas & Germanische Lloyd
HTF	heat transfer fluid
IEA	International Energy Agency
IET	Institute for Energy Systems and Thermodynamics
IPCC	Intergovernmental Panel on Climate Change
IRENA	International Renewable Energy Agency
ORC	organic rankine cycle
PCM	phase change material
PV	photovoltaics
SOC	state of charge
TCES	thermochemical energy storage
TES	thermal energy storage
TFEC	total final energy consumption
TRL	technology readiness level
UNFCCC	United Nations Framework Convention on Climate Change
VRE	variable renewable energy

Roman Symbols

a	thermal diffusivity	$\mathrm{m^2\,s^{-1}}$
c	specific heat capacity	$\mathrm{kJ\,kg^{-1}\,K^{-1}}$
c^*	equivalent specific heat capacity	$\mathrm{kJ\,kg^{-1}\,K^{-1}}$
c_p	specific heat capacity of HTF	$\mathrm{kJ\,kg^{-1}\,K^{-1}}$
E	energy	kJ
G	gibbs free enthalpy	kJ
H	enthalpy	kJ
$H(x)$	Heaviside step function	-
ΔH_R	reaction enthalpy	kJ
h	specific enthalpy	$\mathrm{kJ\,kg^{-1}}$
$\bar{h}$	mean specific enthalpy	$\mathrm{kJ\,kg^{-1}}$
h_0	specific enthalpy at reference temperature T_0	$\mathrm{kJ\,kg^{-1}}$

L	latent heat of fusion	$\mathrm{kJ\,kg^{-1}}$
m	storage material mass	kg
$\dot{m}$	mass flow rate	$\mathrm{kg\,s^{-1}}$
P	power	kW
Q	heat	kJ
q	heat flux	$\mathrm{W\,m^{-2}}$
S	entropy	$\mathrm{kJ\,K^{-1}}$
T	temperature	°C
T^*	dimensionless temperature	-
T_0	reference temperature = 0°C	°C
t	time	s
U	inner energy	kJ
u	velocity	$\mathrm{m\,s^{-1}}$
X	position of the phase front	m

Greek Symbols

Δ	difference operator	
δ	uncertainty operator	
η	similarity variable	
γ	parameter for Stefan problem	
λ	thermal conductivity	$\mathrm{W\,m^{-1}\,K^{-1}}$
ρ	density	$\mathrm{kg\,m^{-3}}$

Subscripts

i	index for discretized section 1 to 3
n	parameter index for polynomial function
Alu	aluminium
app	apparent
el	electrical
f	fusion (syn. melting)
g	gas
HTF	heat transfer fluid
in	inlet
init	initial
l	liquid
loss	losses
lrv	lower range validity
out	outlet
PCM	phase change material
R	reaction
s	solid

sens	sensible
TES	thermal energy storage
th	thermal
urv	upper range validity

Superscripts

liquid	liquid
solid	solid

1. Introduction

In 2015, an overwhelming majority of all the countries around the world adopted the Paris Agreement at the 21st Conference of the parties of the United Nations Framework Convention on Climate Change (UNFCCC), marking a historic turning point in climate change plans. The aim of the Paris Agreement is, to hold the increase of the global average temperature well below 2 °C above pre-industrial levels and pursuing efforts to limit the temperature increase to 1.5 °C above pre-industrial levels [56]. In the course of this adoption, the UNFCCC invited the Intergovernmental Panel on Climate Change (IPCC) to provide a special report on the impact of a global warming of 1.5 °C above pre-industrial levels and related global greenhouse gas emission pathways [29]. A similar analysis had been carried out by the International Energy Agency (IEA) in their flagship report, the *World Energy Outlook* [28].

As pointed out in these reports, the global warming already reached 1 °C in 2017 and will most likely be around 2.5 °C by the end of the century, based on current knowledge and trends. When talking about an increase of the global average temperature it should also be mentioned, that this increase isn't homogeneous for the whole planet. Even though the warming over sea is slightly below the global average, much larger changes are found over land, especially in the high latitudes of the northern hemisphere. In western Siberia the average temperature in the first half of 2020 was 6 °C above the average seen between 1979 and 2019 [9]. A maximum temperature of 38 °C was measured, which is 8 °C above normal temperatures for this region.

Based on the knowledge gained in the reports of the IPCC and the IEA, further investigations where carried out in the *Energy Transition Outlook* [17] by DNV GL and the *Global Renewables Outlook* [31] by the International Renewable Energy Agency (IRENA). Both reports draw pathways which future energy systems have to meet, in order to close the gap between expectations of fast, renewable-driven energy transitions and the reality of today's energy systems.

In this chapter the main findings of the reports mentioned above are summarized and used to explain the necessity and main requirements of energy storage systems.

1.1. Climate Change and Energy Transition

In Figure 1.1 a forecast of the global CO_2 emissions is illustrated for two different energy scenarios.

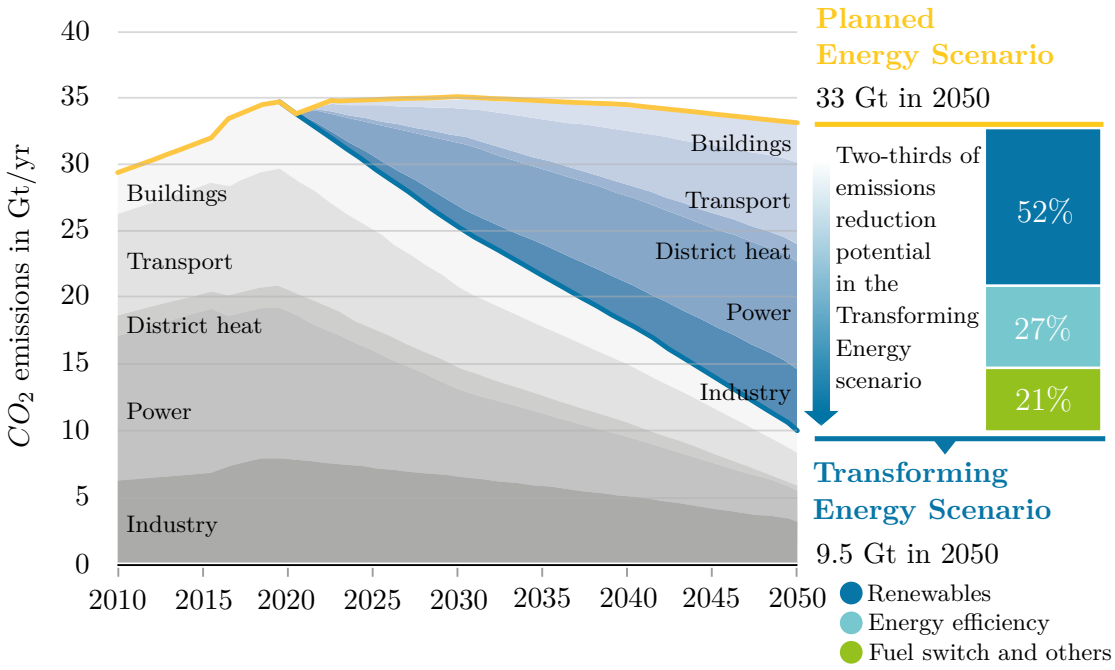

Figure 1.1.: *Energy related CO_2 emissions [31]*

Planned Energy Scenario [31] The Planned energy scenario is based on current energy policy intentions and targets. It illustrates the consequences if CO_2 emissions peak in 2030 and then slightly decline to 33 Gt in 2050 (approx. today's level). This scenario would result in a rise of the global average temperature of about 2.5 °C in the second half of this century. In other publications this scenario is also called the Stated Policies Scenario [28].

Transforming Energy Scenario [31] This scenario is comparable to the Sustainable Development Scenario in the IEA's *World Energy Outlook* [28]. It represents a pathway needed to keep the rise of the global average temperature well below 2 °C above pre-industrial levels. To achieve these goals, the global CO_2 emissions have to fall by 3.8% per year, which leads to 70% less emissions in 2050 compared to the Planned Energy Scenario.

As shown in Figure 1.1, in the transforming energy scenario more than half of the reductions in CO_2 emissions can be accomplished by the transition of the energy system to renewable energy sources. The second half comes from energy efficiency and the switch to eco-friendly fuels like green hydrogen.

1.1.1. Renewable Energy

In the Transforming Energy Scenario, electricity becomes the central energy carrier with a share of about 50% of the final energy consumption. This will lead to a gross electricity consumption which is more then twice as high as today's (20% in 2017). In addition to this drastic increase of the electricity demand, the share of renewables in electricity generation has to rise from currently 25% to about 86% in 2050 (see Figure 1.2), which means adding over 520 gigawatts of renewable energy capacity every year.

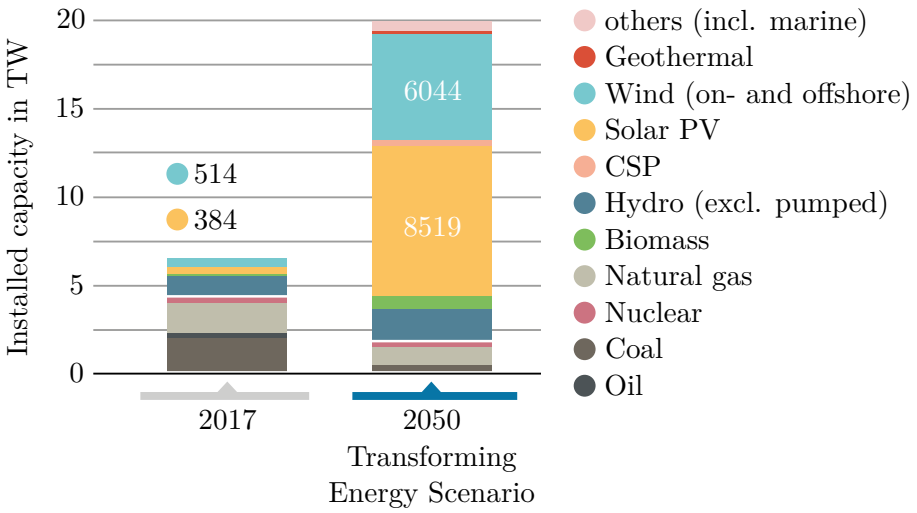

Figure 1.2.: *Total installed capacity for electricity generation [31]*

However, variable renewable energy sources (VRE) like solar PV and wind tend to be unpredictable and are subject to seasonal and daytime-dependent fluctuations. Therefore it won't be enough to only increase the share of renewables in the total final energy consumption (TFEC). The higher the share of renewables in a power system the more flexibility needs to be added to it. Some options to increase the flexibility of a grid with a large share of VRE's are [17]:

- Energy storage: Short-term as well as long-term storage systems can minimize the temporal discrepancy between energy demand and -supply.
- Expanding the grid: Smoothing variability and improving robustness to failures by improving connections between neighbouring grids.

- Flexible generation: Use generators with the ability to start quickly and vary their output rapidly.
- Flexible demand: Reducing power consumption at peak times.
- Flexible markets and regulation: Increase the flexibility of the markets to enable power systems to operate efficiently.

Of all the aspects mentioned above, energy storage is the one with the biggest potential to increase the flexibility of future power grids. That is why the global storage capacity available to the grid has to increase from 8 GWh [27] today to nearly 45 TWh [17] in 2050.

1.1.2. Energy Efficiency

As already mentioned in this section and shown in Figure 1.1, the goals presented in the Transforming Energy Scenario can't be reached by the transition of the global energy system to renewables only. More than a quarter of the reductions in CO_2 emissions in 2050 should come from energy efficiency improvements. Industry and power generation are two sectors with the biggest potential in terms of energy efficiency improvements. Increasing energy efficiency in the industry sector means increasing waste heat recovery in industrial processes. Again, energy storage systems can play a key role in reaching this targets. Most industrial processes, for example in the iron and steel industry, are batch-processes, which means a discontinuous operation mode and hence a temporal discrepancy between heat demand and waste heat supply. The integration of energy storage systems in such batch-processes can help improving the energy efficiency by bridging this temporal discrepancies.

In the power generation sector modern combined heat and power (CHP) plants are operated as heat demand following processes [41]. This operation strategy avoids waste heat by first covering the heat demand and then buying or selling electricity in order to integrate the rest of the energy demand or supply with the drawback of a bad thermal efficiency of the power cycle. The best thermal efficiency of the power cycle could be reached by a electricity demand following operation strategy. In such an operation mode the system would first cover the electricity demand and then provide the rest of the energy needs by using auxiliary heating or by wasting heat. As before, energy storage systems are suitable to compensate this auxiliary heating- and waste heat problem.

1.2. Thermal Energy Storage Systems

Thermal energy storage (TES) systems are storage types where energy is stored in the form of heat. This heat can either be sensible, latent or even heat in form of the reaction enthalpy of a reversible chemical reaction. A sensible heat TES is characterized by a significant change of the storage temperature between the initial temperature T_{init} and the final temperature T_{final} during charging and discharging. For a constant specific heat of the storage material, the correlation between the storage temperature and the

stored energy is linear, as it is shown in Figure 3.4. Therefore, the capacity of a sensible heat TES, in addition to the specific heat of the storage material, also depends on the temperature range $T_{\text{final}} - T_{\text{init}}$. In contrast to this, latent heat TES enable high capacities even at small temperature differences. They take advantage of energy that is consumed or released during a phase change. As visualized in Figure 3.4 the temperature in a latent heat TES stagnates at a certain temperature even though the stored energy is still rising, which is due to the latent heat of the phase change. These characteristics lead to high storage densities and hence reduced storage volumes of latent heat TES. Storage types where thermal energy is stored by making use of a reversible chemical reaction or a sorption process are called thermochemical energy storage systems (TCES). During a sorption process heat is released at a constant temperature, which allows storing a large amount of heat in a narrow temperature interval, similar to latent heat TES. The temperature of the heat released or consumed during a reversible chemical reaction is not latent, but depends on the reaction conditions. By changing the partial pressure of one reaction component, the reaction temperature can be adjusted, allowing to release heat at higher temperatures than it had been stored before (concept of a chemical heat pump).

A majority of utility-scale TES in 2018 account to molten salt storage systems in CSP-plants [18]. Concentrated solar power (CSP) is a technology which uses heat provided by concentrated solar irradiation to operate a Clausius-Rankine power cycle for electricity generation. As every technology which makes use of solar energy, the electricity output of such a power plant is highly volatile. For this reason modern CSP-plants are enhanced by incorporating thermal energy storage systems. An overview on modern CSP technologies and the integration of TES systems is given by Zhang et al. [63] and Pelay et al. [48]. As Pelay et al. stated in their work, high temperature latent heat TES would make, due to their high energy densities, a good fit for the integration in CSP-plants, if their weren't the drawbacks of low thermal conductivity of the phase change material (PCM) and the high volatile power rates. Both problems could be solved by the results of the research carried out in the course of this work.

1.3. Selected Experimental Investigations

This section presents a selection of investigations which are currently carried out on latent heat TES dealing with comparable PCM's and heat exchanger designs than the ones utilized for this work.

1.3.1. German Aerospace Center

At the German Aerospace Center (DLR) lots of latent heat test rigs had been erected to study their applicability in CSP-plants and industrial processes. Currently a 1.5 MW h_{th} latent heat TES for the integration in a co-generation plant is under construction [39]. The storage is capable of producing superheated steam at over 21 bar and 200 °C for at least 15 minutes, resulting in power rates of over 6 MW_{th}. In the storage aluminium fins with a design similar to the ones used in this work are chosen as heat transfer enhancement and approximately 32 tons of sodium nitrate are utilized as PCM. In Figure 1.3 the integration of the latent heat TES is shown schematically. Some recommendable articles in this context are [37], [38], [36] and [39].

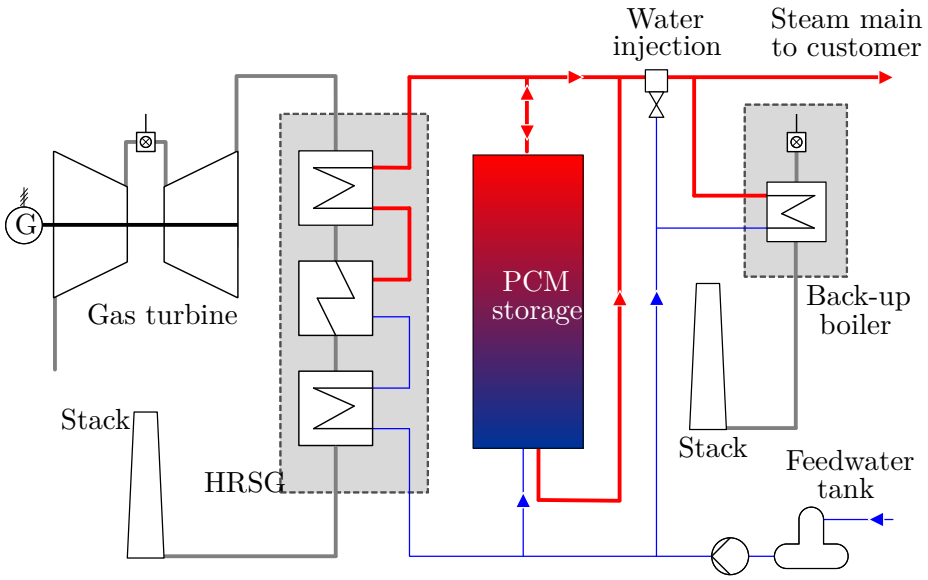

Figure 1.3.: *Integration of the latent heat TES in the co-generation plant at DLR [37]*

1.3.2. Ghent University

At Ghent University a latent heat TES with an eutectic mixture of sodium nitrate and potassium nitrate as storage material is examined. The TES is integrated in an ORC-waste-heat-recovery process to mitigate the fluctuations in waste heat availability which avoids partial load operation of the ORC. The test rig consists of a 110 kW h_{th} latent heat TES which supports a 11 kW_{el} ORC unit. More detailed information on the

experimental work at Ghent University can be found in the articles of Couvreur et al. [58], [12] and [13]. In Figure 1.4 the integration of a TES in an ORC for waste heat recovery available from a continuous annealing furnace and galvanization line is shown.

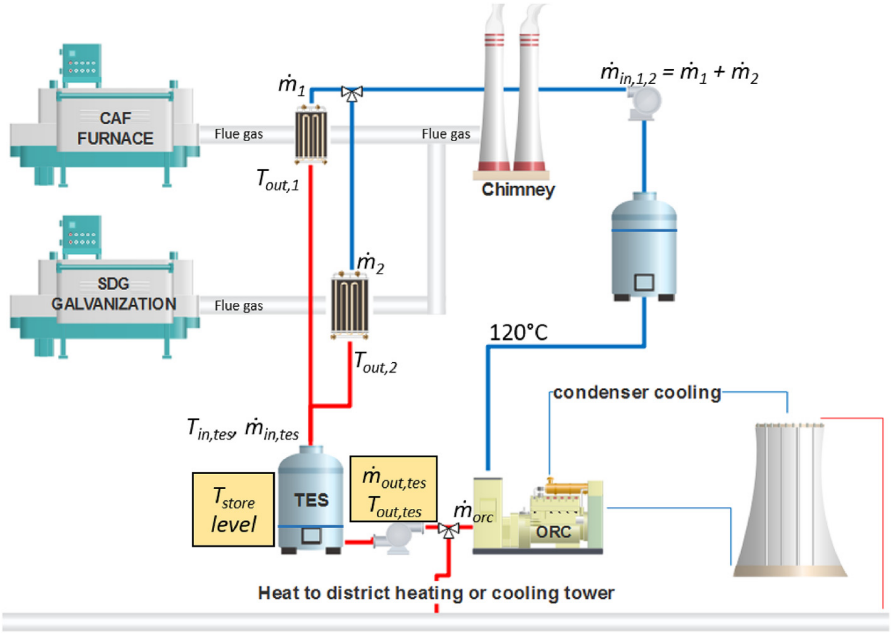

Figure 1.4.: *Integration of the latent heat TES in an ORC for waste heat recovery available from a continuous annealing furnace and galvanization line [13]*

1.3.3. University of Lleida

A low temperature latent heat TES with high density polyethylene as PCM is examined at the University of Lleida. The test rig consist of a 0.304 m^3 storage tank with horizontal U-shaped tubes which act as the heat exchanger surface. The storage is filled with 99.5 kg of PCM which results in a storage capacity of about 10 $kW\,h_{th}$. Similar to the investigations carried out in this work the team at the University of Lleida also focused on partial cycle operation modes of the TES. The first experiments on partial cycle operation modes were carried out in 2018 without using any heat transfer enhancing method. Results of these experiments showed that partially charging a TES has an influence on the discharging process which is a big disadvantage when predicting the power rates in a latent heat TES. Based on these findings a smaller test rig has been constructed to examine the influence of several heat transfer enhancing methods on partial cycle operation modes of latent heat TES. Comprehensive articles in this course are [23], [22] and [21].

2. Scope of Work and Research Question

Regarding the matters mentioned in the end of Section 1.2, a high temperature latent heat thermal energy storage system which could be utilized to increase the efficiencies of modern CSP- and CHP-plants, is examined in this work. The test rig mainly consists of a vertically mounted shell and tube heat exchanger where the heat transfer fluid is flowing inside the inner tube and the volume between the shell and the tube is filled with PCM (sodium nitrate). To improve the heat transfer and hence the power rates of the TES, a combination of arborescent longitudinal and transversal aluminium fins is applied to the heat exchanger tube in the examined test rig. Detailed informations about the properties of the storage material and the geometry of the test rig are given in Section 4.1.

For the characterization of a storage system it is crucial to have knowledge about the actual amount of energy which is stored at a certain time. For sensible heat TES this can easily be accomplished by measuring the temperature of the TES and using Eq. (3.1) to calculate the stored energy. Because of a different storing principle (storing energy at a constant temperature) this method can not directly be applied to latent heat TES.

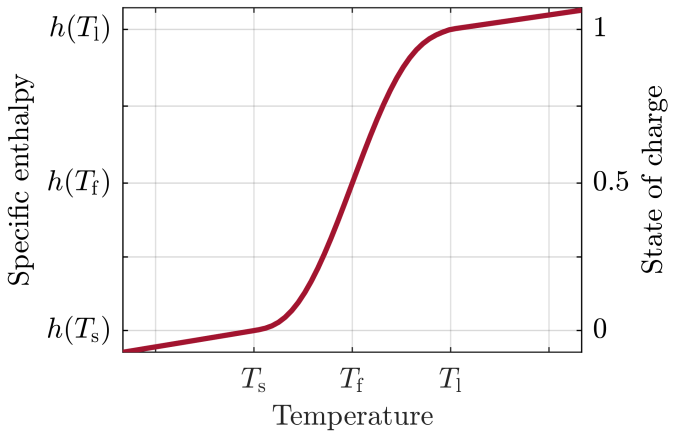

Figure 2.1.: *Correlation between SOC, spec. enthalpy and temperature*

Therefore the so called state of charge (SOC) is defined for the characterization of the examined TES. For the experimental investigations the TES is operated between a specific temperature range (lower limit = T_s, upper limit = T_l) around the melting point of sodium nitrate. The latent heat of fusion is distributed over this temperature range

which results in a steady and hence integrable enthalpy function. Using this enthalpy distribution function the definition of the SOC is formulated in a way that the SOC is 0 if the average temperature of the PCM is equal to T_s and 1 if the average temperature of the PCM is T_l. In Figure 2.1 the correlation between the three variables state of charge, specific enthalpy and temperature is displayed.

Lots of experiments had been carried out on latent heat TES and their power rate problem. However, the only publications on the partial cycle operation of latent heat TES found, to the best of the authors knowledge, are two studies from Gasia et al. ([23] and [22]). In their first paper Gasia et al. examine a low temperature latent heat TES with a different storage type and PCM than the one examined in this work. They added storage time to their research as an additional complexity factor in the second paper. The results of their research correspond to Groulx's 'rate problem' [25] showing steadily declining power rates immediately after starting to discharge the storage.

This is due to the fundamentally different heat transfer mechanisms which are dominant at solidification and melting processes. During solidification, the heat transfer surface is covered with solid PCM immediately after starting to discharge, leading to a conduction-based heat transfer for further solidification. The opposite effects apply to the melting process which results in a convection-based heat transfer during melting. For a better understanding of this problem the phenomena just explained are visualized in Figure 2.2 for three different operation cycles.

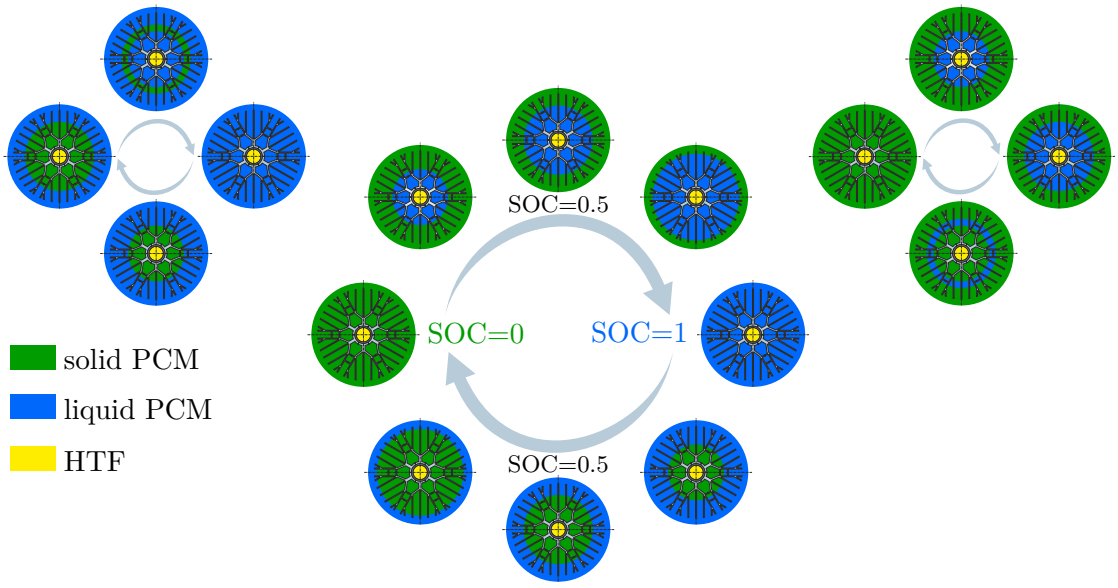

Figure 2.2.: *Schematic SOC: full cycle (center), partial cycle between* $SOC = 0.5$ *and* $SOC = 1$ *(top left), partial cycle between* $SOC = 0$ *and* $SOC = 0.5$ *(top right)*

Due to the low thermal conductivity of sodium nitrate, low power rates are expected for high fractions of solid PCM during discharging. In order to evaluate the efficiency of the novel fins introduced in [52] for partial cycle operation modes the following experimental investigations had been carried out within this work:

- Formulate a distribution function for the latent heat of fusion.
- Formulate a definition of the state of charge.
- Determine the power rates for different partial and full load cycles in dependence of the SOC.
- Compare the PCM-based SOC with the HTF-based SOC in order to validate the measured data.

The results of these investigations are used to address the following research questions in Chapter 5:

- Is the definition of the state of charge presented in Section 4.3 suitable for the characterization of the examined latent heat TES?
- Are the utilized aluminium fins a suitable heat transfer enhancement method to the examined latent heat TES?
- How does the power rate correlate to the state of charge in various partial cycle operation modes?

3. Theoretical Framework

As already mentioned in Chapter 1, energy storage systems will play a key role in increasing flexibility and reliability of future power systems. In this chapter an overview on state of the art storage technologies is given. Especially the use of phase change materials in latent heat TES systems as well as the difficulties that are involved, when using PCM as a storage material, are discussed.

3.1. Energy Storage Systems

At the time a variety of different technologies for storing energy is available. Each one suitable for different applications and available at different technology readiness levels (TRL). For a energy storage system to have potential for marketability, it must meet the following requirements:

- high efficiency
- high storage density
- environmentally friendly
- high power rates (at full- and partial cycle operating conditions)
- scalable
- cost-efficient
- wide range of applications
- emission-free
- high TRL

In Figure 3.1 an overview on global operating energy storage power capacity is given. As can be seen, pumped hydro plants account for more than 90% of the installed storage capacity in 2017. 75% of the installed thermal storage capacity are molten salt thermal storage systems, which are often used in modern CSP-plants.

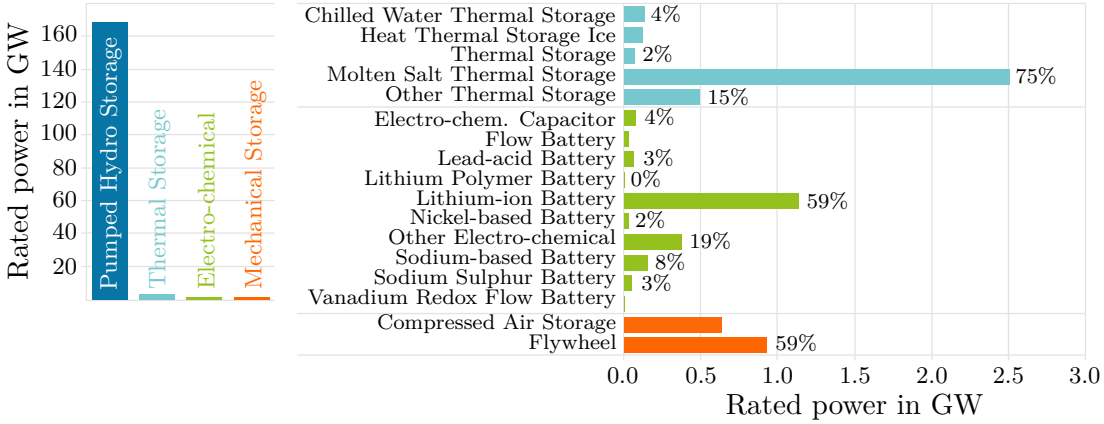

Figure 3.1.: *Global operational storage power capacity by technology in mid 2017 [33]*

3.1.1. Mechanical Energy Storage

Pumped-hydro plants are the most mature and widely spread (170 GW installed capacity worldwide in 2019 [32]) energy storage systems with the prediction of further noticeable growth in the next decades [17]. Together with compressed air energy storage (CAES) systems pumped-hydro is the only technology available at the moment which is capable of storing big amounts of energy in a energy- and cost-efficient way [33]. Both technologies make use of the pressure difference between two reservoirs and a massive storage volume to store large amounts of energy with high power rates and efficiencies.

In a pumped-hydro plant a so called pump-turbine (can operate as a pump or a turbine) is used to pump water from a lower reservoir to an upper reservoir when too much electricity is available to the grid. In times of high electricity demand, the pump-turbine is driven by the water flowing from the upper reservoir to the lower reservoir, thereby generating electricity again.

In CAES systems the low pressure reservoir is the surrounding atmosphere and as high pressure reservoir salt caverns or artificially built rock caverns could find use. For charging a CAES the air from the surrounding is compressed in a turbo compressor and then stored in an underground pressurized cavern. To discharge a CAES the compressed air is used to drive a turbine which in turn generates electricity. For this simple type of CAES, a so called diabatic CAES, efficiencies of about 50% can be reached, which is not very satisfying. To increase the efficiency of a CAES system it needs to be coupled with a thermal energy storage which leads to the second type of CAES systems, the adiabatic CAES. In such a system the TES is used to store the thermal energy which is produced during the compression of the surrounding air in the charging mode. During the discharging mode, the stored thermal energy is used to heat to compressed air before it is expanded, to increase the power output of the turbine. The efficiency of an adiabatic CAES system is expected to be around 70%.

However, for both technologies geological basic requirements like mountains and the existence of salt caverns are mandatory for their application in a certain region. This fact limits the area of application of these two technologies only to a few countries and regions around the globe.

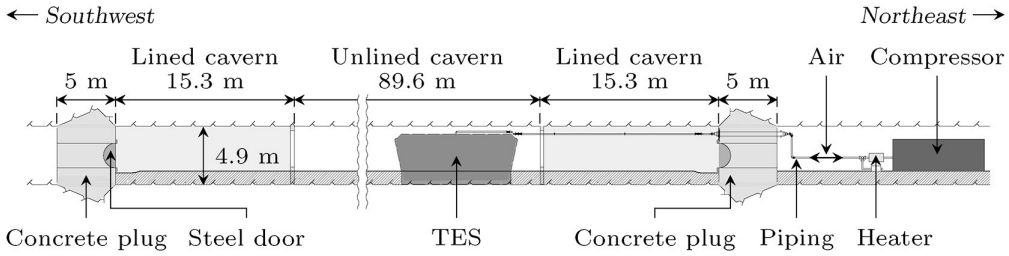

Figure 3.2.: *Schematic of the test rig at ETH Zürich [24]*

At the time writing this thesis only three utility scale CAES plants were built. Two CAES in its simpler form, the diabatic CAES, exist in Huntorf, Germany (321 MW_{el}, since 1978), see Crotogino et al. [15] and [14] and McIntosh, USA (110 MW_{el}, since 1991), see Nakhamkin et al. [46] and Daly et al. [16]. The world's first advanced adiabatic CAES was constructed by a research group at the ETH Zürich inside a mountain tunnel in the swiss alps. The CAES is supported by a 11.6 MW h_{th} sensible- and a 171.5 kW h_{th} latent heat TES. The overall round-trip efficiency of the pilot plant is expected between 63-74% (see Geissbühler et al. [24] and Becattini et al. [7]). A schematic of the whole experimental setup is shown in Figure 3.2.

3.1.2. Electrochemical Energy Storage

According to the reports discussed in Chapter 1 electrochemical energy storage systems will experience a dramatic growth in the next few years. Technologies with the most potential in this sector are lithium-ion batteries and flow batteries. As shown in Figure 3.1, lithium-ion batteries already account for nearly 60% of the installed electrochemical storage capacity in 2017. A executive summary on electricity storage (especially battery storage) is provided in the IRENA-report [30].

In lithium-ion batteries the difference in the electrochemical potentials of two lithium intercalation compounds, which represent the electrodes, is used to store electric energy in a safe and efficient way. Flow batteries are based on reversible elektrochemical reactions and are therefore often described as regenerative fuel cells. Different from lithium-ion batteries the electroactive materials are not stored within the electrodes but in separate tanks. For charging and discharging the electrolytes are pumped into the reaction unit where the reversible electrochemical reaction occurs. In Table 3.1 the most important advantages and disadvantage of both technologies are summarized.

Table 3.1.: *Advantages and disadvantages of lithium-ion and flow batteries [30]*

Advantages	**Disadvantages**
Lithium-ion batteries	
• high specific energy • high energy and power density • high power discharge capability • excellent round-trip efficiency • low self discharging rate	• moderate safety characteristics • lack of thermal stability • moderate cycle life
Flow batteries	
• operate close to ambient temperature • energy and power are independently scalable • high cycle lifetimes • uses inexpensive raw materials • good safety characteristics	• potential leakage of acidic solutions • need for sensors, pumping and flow management mechanisms • high cost of some key system elements

3.2. Thermal Energy Storage

Especially when talking about waste heat recovery and flexibility of power systems with a high share of variable renewable energy sources, thermal energy storage systems are the ones with the most potential. An executive overview on thermal energy storage systems and their applications is given by Alva [3] and Zhang [66]. Depending on the application and the storage time, there are three main technologies for thermal energy storage systems.

3.2.1. Sensible Heat TES

In sensible heat TES systems a single phase material is used as storage material. This storage material can either be solid, liquid or, less common, gaseous. The capacity of sensible heat TES mainly depends on the specific heat of the storage material and the difference between the initial and final temperature of the storage, as it is visualized in Eq. (3.1).

$$E = \int_{T_{\text{init}}}^{T_{\text{final}}} m\, c\,(T)\, \mathrm{dT} \tag{3.1}$$

The temperature of a sensible heat TES rises when charging, and reverse for discharging. Representatives for this technology are:

Ruths Steam Accumulator A pressurized vessel, filled with a water/steam mixture, is charged by adding superheated steam at high pressures and discharged by removing steam at low pressures. Ruths steam accumulators are simple, robust storage systems but suffer big exergy losses due to the temperature difference between the two-phase mixture in the storage and the superheated steam which is used for charging.

Packed Bed Regenerator The most common storage materials in packed bed regenerators are gravel and rocks. Hot air or any other type of gas acts as HTF which flows through the gaps between the gravel stones. For packed bed regenerators it is crucial to choose the particle size of the storage material in a way that the surface of the particle (hence the heat exchanger surface) is maximized and the pressure losses in the HTF are minimized. Because these are two opposite phenomena, several experimental investigations had been carried out in this course at IET in the last few years.

Active Fluidized Bed Sand TES In this type of storage fine sand is used as storage material. The whole system mainly consists of a cold storage tank, a hot storage tank and a fluidized bed with a horizontal pressure drop (which leads to the horizontal transport of the storage material from one storage tank to the other). During charging, the sand is transported from the cold storage tank, through the fluidized bed, to the hot storage tank and reverse for discharging. When flowing through the fluidized bed, the sand is heated by a HTF which is flowing in immersed heat exchanger tubes. In order to find

the best operational parameters as well as the best design and arrangement of the heat exchanger tubes, lots of experimental investigations had been carried out at IET in the last couple of years. A process flow diagram of the test rig examined at IET is shown in Figure 3.3.

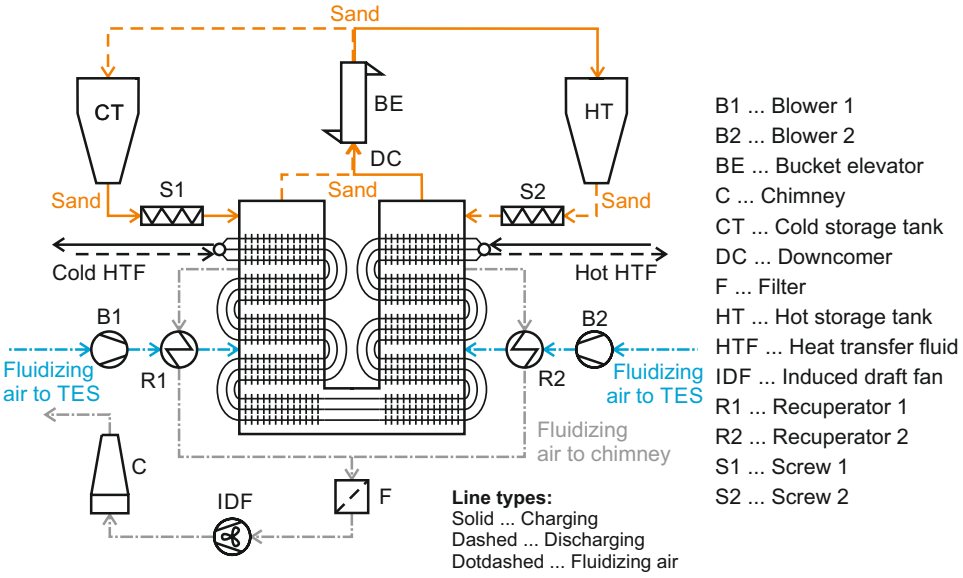

Figure 3.3.: *Process flow diagram of the fluidized bed sand TES at IET*

Molten Salt Storage As already mentioned in Chapter 1, the power generation in conventional CSP-plants strongly depends on the daytime. With a storage system of this type CSP-plants are enabled to generate electricity continuously. During the day, the solar energy is used to produce steam for electricity generation and to heat up the salt in the storage. During night, when no solar energy is available, the heat stored in the molten slat storage is used to produce the steam needed for electricity generation.

3.2.2. Latent Heat TES

In latent heat TES so called phase change materials are used as storage material. In contrast to sensible heat TES the temperature in a latent heat TES ideally does not change during charging or discharging. This is because latent heat TES use the heat of fusion at isobaric conditions to store thermal energy. This leads to some advantages and disadvantages compared to other technologies:

- High storage density and hence a reduced storage volume.
- Low exergy losses when storing latent heat (evaporation/condensation).
- During a solid/liquid-phase change the volume increases by about 10-20%.
- Poor nucleation behaviour, and hence the risk of subcooling.
- Low thermal conductivity of the solid PCM.

$$E = \underbrace{\int_{T_{\mathrm{init}}}^{T_{\mathrm{f}}} m\, c_{\mathrm{s}}\,(T)\ \mathrm{dT}}_{\text{sensible heat (solid)}} + \underbrace{m\, L}_{\text{latent heat}} + \underbrace{\int_{T_{\mathrm{f}}}^{T_{\mathrm{final}}} m\, c_{\mathrm{l}}\,(T)\ \mathrm{dT}}_{\text{sensible heat (liquid)}} \tag{3.2}$$

In practice, latent heat TES are not only operated at a constant temperature, but also between a specific temperature range around the phase change. In this work this temperature range is defined by the initial temperature T_{init} and the final temperature T_{final}. With this definition, the capacity of a latent heat TES can be calculated like it is shown in Eq. (3.2). The storage capacity of a latent heat TES with a solid/liquid phase change therefore consists of the sensible heat in the solid region, the latent heat of fusion and the sensible heat in the liquid region. Figure 3.4 presents a comparison of the temperature trends in a sensible- and latent heat TES during a charging process. Detailed informations on latent heat TES and the use of phase change materials as storage materials are provided by Sharma [55] and Nazir et al. [47].

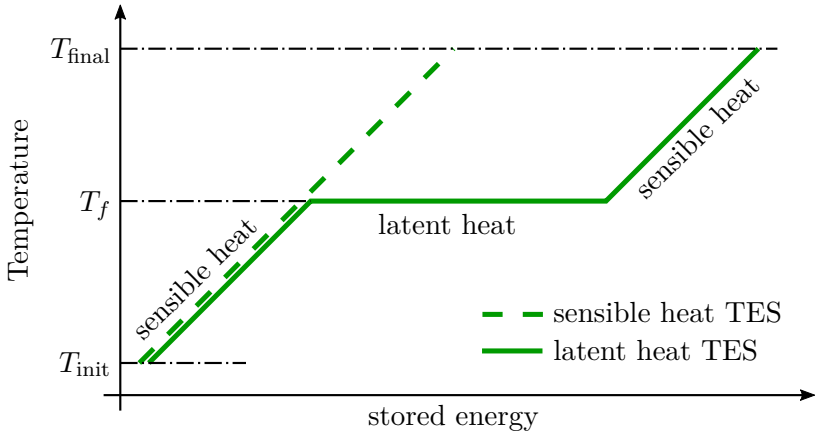

Figure 3.4.: *Storage behaviour: sensible vs. latent heat TES*

3.2.3. Thermochemical Energy Storage

The term thermochemical energy storage means concepts for the storage of heat that are based on a sorption process or a reversible chemical reaction. Absorption and adsorption processes are sometimes also physical processes, but these technologies are also referred to as thermochemical storage systems. Zeolites, for example, can be used as storage materials in these sorption technologies. In most thermochemical storage systems, the reaction enthalpy of a reversible gas/solid reaction is used to store heat in the form of chemical energy. Such a reaction can generally be described by the following reaction equation Eq. (3.3):

$$A_{(s)} + \Delta H_R \rightleftharpoons B_{(s)} + C_{(g)} \tag{3.3}$$

A solid component A is selected as the storage material, which reacts to a solid component B and a gaseous component C by consuming heat. Heat can therefore be stored to the extent of the reaction enthalpy ΔH_R. Due to the easy separability of solid and gaseous substances, this storage process can take place almost without any loss, even over very long periods. To discharge the storage, the two components B and C are brought together again. They react to the starting component A, thereby releasing the reaction enthalpy in the form of heat [8].

3.3. Phase Change Materials

Phase change materials typically are materials that undergo a solid/liquid phase transition at a certain temperature within the temperature range of a selected thermal application. Therefore only the fundamentals of a first order solid/liquid phase transition are attended in this chapter.

3.3.1. Phase Change Phenomena

From a thermodynamic point of view, the gibbs free enthalpy is a particularly important function in order to study the fundamentals of a phase change. For a pure substance the gibbs free enthalpy of a single phase and its first derivative with respect to the temperature T can be written as

$$G = H - TS \qquad \left(\frac{\partial G}{\partial T}\right)_p = -S. \tag{3.4}$$

Every thermodynamic system tends to minimize this gibbs free enthalpy since this is the most stable configuration. Therefore the temperature-dependence of the gibbs free enthalpy is of interest when intending to make a statement about the reason for a phase change. So as to minimize the gibbs free enthalpy, the enthalpy has to be minimized and the entropy has to be maximized. At low temperatures the enthalpy term is dominant, for high temperatures the entropy term is. This means that at high temperatures the phase with the higher entropy is going to be more stable. The resulting temperature dependency of the gibbs free enthalpy in the region of a solid/liquid first order phase transition is shown in Figure 3.5a.

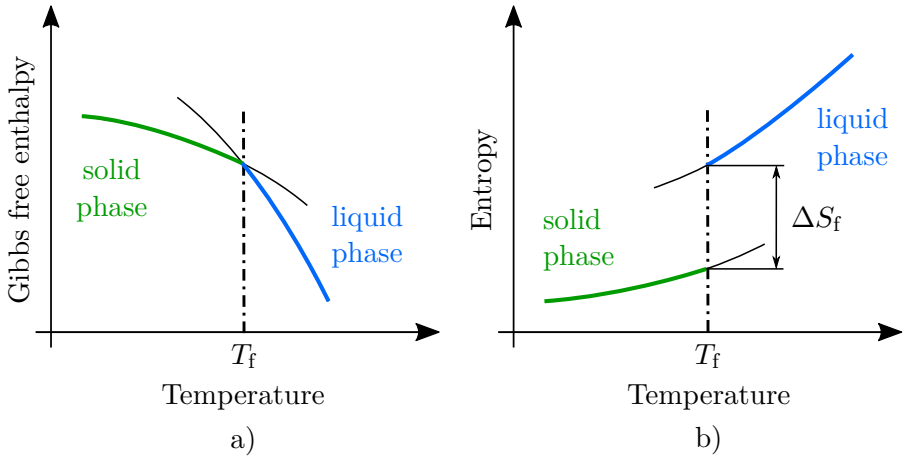

Figure 3.5.: *Gibbs free enthalpy (a) and entropy (b) of a solid/liquid first order phase transition*

As Fleischer [20] states in her book, the entropy of the liquid phase is, due to the higher vibration states of the constituent molecules, higher than the entropy of the solid phase. This fact is visualized by a different slope of the gibbs free enthalpy and a finite discontinuity of the entropy (first derivative of the gibbs free enthalpy) in Figure 3.5. For given values of the temperature T and the pressure p, the equilibrium state is the one with the lowest gibbs free enthalpy. At the melting temperature the $G(T)$ trends intersect ($G^{\text{solid}} = G^{\text{liquid}}$), which leads to an equilibrium state where both phases (solid and liquid) coexist. Therefore the latent heat of fusion which is consumed or released during such a first order phase transition can be written as

$$L = \Delta G + T_\text{f}\,\Delta S_\text{f} = T_\text{f}\,\Delta S_\text{f} \qquad \left(\Delta G = G^{\text{liquid}} - G^{\text{solid}} = 0\right). \tag{3.5}$$

3.3.2. Modelling the Phase Change

When examining a latent heat TES, a mathematical description of the phase change is of interest. Analytical solutions of this problem, the so called Stefan problem, are only available for certain geometries and do not take the heat transfer due to natural convection in the liquid phase into account.

The Stefan Problem - Analytical Solution

The Stefan problem is the simplest (one-dimensional) mathematical model to describe a phase transition. It aims to model the solidification process of a homogeneous fluid in a half-infinite volume. This volume is limited by a wall with an initial temperature T_0. A schematic of this problem is shown in Figure 3.6. The initial- and boundary conditions are:

$$T(x,0) = T_0, \quad T(0,t>0) = T_1 < T_f, \quad T(x\to\infty,t) \to T_0 \tag{3.6}$$

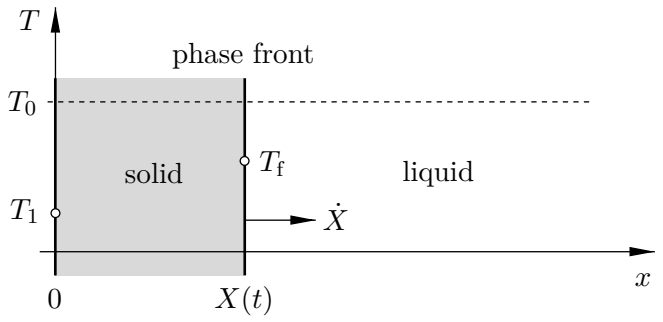

Figure 3.6.: *Stefan problem*

With the assumption of incompressible fluids and Fourier's law the energy balance for the solid phase simplifies to

$$\frac{\partial T_\mathrm{s}}{\partial t} = a_\mathrm{s}\,\frac{\partial^2 T_\mathrm{s}}{\partial x^2}, \qquad a_\mathrm{s} = \frac{\lambda_\mathrm{s}}{\rho_\mathrm{s}\,c_\mathrm{s}}. \tag{3.7}$$

This equation (Eq. (3.7)) is also referred to as the heat equation. For the solution of this second order differential equation a dimensionless temperature T^* and a similarity variable η_s are defined (see Eq. (3.8)).

$$T^* = \frac{T - T_\mathrm{l}}{T_0 - T_\mathrm{l}}, \qquad \eta_\mathrm{s} = \frac{x}{\sqrt{4\,a_\mathrm{s}\,t}} \tag{3.8}$$

With these two definitions, the boundary condition at x=0 (t>0) and the temperature at the phase front ($T = T_\mathrm{f}$), the dimensionless temperature in the solid phase T_s^* and the position of the phase front $X\,(T)$ can be written as

$$T_\mathrm{s}^*\,(\eta_\mathrm{s}) = \frac{T_\mathrm{f}^*}{\operatorname{erf}\gamma}\,\operatorname{erf}\,(\eta_\mathrm{s})\,, \qquad X\,(T) = \gamma\,\sqrt{4\,a_\mathrm{s}\,t} \tag{3.9}$$

Analogous to Eq. (3.7) the energy balance for the liquid phase simplifies to Eq. (3.10).

$$\frac{\partial T_\mathrm{l}^*}{\partial t} + u_\mathrm{l}\,\frac{\partial T_\mathrm{l}^*}{\partial x} = a_\mathrm{l}\,\frac{\partial^2 T_\mathrm{l}^*}{\partial x^2}, \qquad a_\mathrm{l} = \frac{\lambda_\mathrm{l}}{\rho_\mathrm{l}\,c_\mathrm{l}}. \tag{3.10}$$

This time the heat equation also includes a convective term which is due to the different densities of the solid and liquid phase. The continuity of the mass flux at the solid/liquid interface, a conclusion from the integral mass balance, is used to find the velocity of the liquid phase.

$$u_\mathrm{l} = \frac{\rho_\mathrm{l} - \rho_\mathrm{s}}{\rho_\mathrm{l}}\,\frac{\mathrm{d}X}{\mathrm{d}t} \tag{3.11}$$

With Eq. (3.11), the similarity variable $\eta_\mathrm{l} = x/\sqrt{4\,a_\mathrm{l}\,t}$, the boundary condition at $x \to \infty$ and the temperature at the phase front ($T = T_\mathrm{f}$) the dimensionless temperature in the liquid phase T_l^* can be expressed as

$$T_\mathrm{l}^*\,(\eta_\mathrm{l}) = 1 - (1 - T_\mathrm{f}^*)\,\operatorname{erfc}\left(\eta_\mathrm{l} - \gamma\,\frac{(\rho_\mathrm{l} - \rho_\mathrm{s})}{\rho_\mathrm{l}}\sqrt{\frac{a_\mathrm{s}}{a_\mathrm{l}}}\right)\,\operatorname{erfc}^{-1}\left(\gamma\,\frac{\rho_\mathrm{s}}{\rho_\mathrm{l}}\sqrt{\frac{a_\mathrm{s}}{a_\mathrm{l}}}\right). \tag{3.12}$$

For the determination of the yet unknown parameter γ in Eq. (3.9) and Eq. (3.12) the interface condition for the phase front

$$-\,(q_\mathrm{l} - q_\mathrm{s}) = \rho_\mathrm{s}\,\frac{\mathrm{d}X}{\mathrm{d}t}\,\underbrace{(h_\mathrm{l} - h_\mathrm{s})}_{-L} \tag{3.13}$$

which is also referred to as the Stefan condition is used. In combination with Fourier's law Eq. (3.13) results in

$$-\,\lambda_\mathrm{l}\,\frac{\partial T_\mathrm{l}}{\partial x}\bigg|_{x=X} + \lambda_\mathrm{s}\,\frac{\partial T_\mathrm{s}}{\partial x}\bigg|_{x=X} = \rho_\mathrm{s}\,\frac{\mathrm{d}X}{\mathrm{d}t}\,L. \tag{3.14}$$

The expansion of Eq. (3.14) with Eq. (3.9) and Eq. (3.12) leads to a transcendent Equation which has to be solved numerically to determine the unknown parameter γ.

3.3.3. Heat Transfer Enhancement Methods

The major problem of latent heat TES is the low thermal conductivity of the utilized PCM's. Jegadheeswaran et al. [34] provide a good overview on research works which had been conducted in this context. Overall there are four main technologies to improve the heat transfer in PCM's and thereby the power rates of latent heat TES:

Extension of the Heat Exchanger Surface

During a solidification process in a latent heat TES, heat is transferred from the PCM to the heat exchanger surface. The PCM first starts to solidify at the surface of the heat exchanger, leading to a conduction-dominant heat transfer mechanism for further solidification. Steadily declining power rates at higher fractions of solid PCM are a result of this behaviour. A possible option to accomplish high power rates even at high fractions of solid PCM is to increase the heat exchanger surface by applying fins.

Contrary to a solidification process, during a melting process the heat transfer is conduction-dominant only at the beginning when all of the PCM is solid. As soon as the PCM starts to melt, natural convection kicks in, increasing the heat transfer significantly, according to [34]. As to allow natural convection during the melting process Walter et al. [60] found that for a vertical heat exchanger tube longitudinal fins would be the best match. Popular arborescent longitudinal fin types suitable for tube heat exchangers are shown in Figure 3.7. Recommendable articles on finned shell and tube latent heat TES are the ones from Lacroix [43], Zhang [67], Guo [26] and Choi [11].

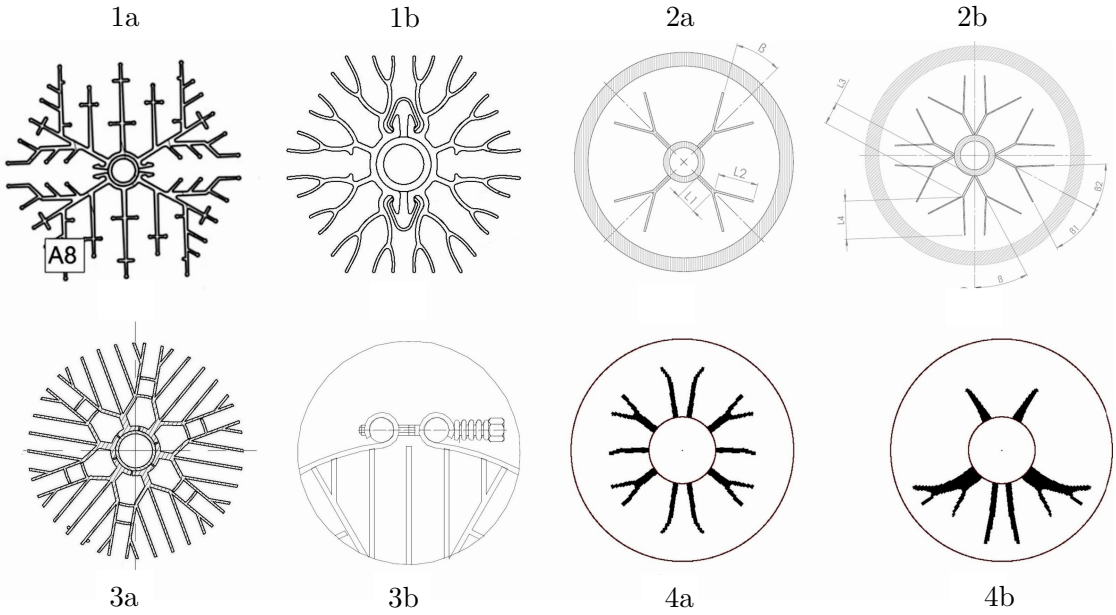

Figure 3.7.: *Arborescent longitudinal fins types: 1a from [6], 1b from [35], 2a & 2b from [54], 3a from [52], 3b from [50], 4a & 4b from [49]*

Combination of Multiple PCM's

One driving force of the heat transfer in a latent heat TES is the temperature difference between the HTF and the PCM. For a heat source/sink with a finite heat capacity the temperature difference between the HTF and the PCM decreases in the flow direction of the HTF leading to a bad performance of the TES. When packing the latent heat TES with different types of PCM, each having a distinct melting temperature, a constant temperature difference between HTF and PCM could be maintained. Comprehensive investigations on this enhancement technology had been carried out by Wang et al. [61], Farid et al. [19] and Michels et al. [45]. The use of the combination of multiple PCM types in a shell and tube latent heat TES is shown in Figure 3.8.

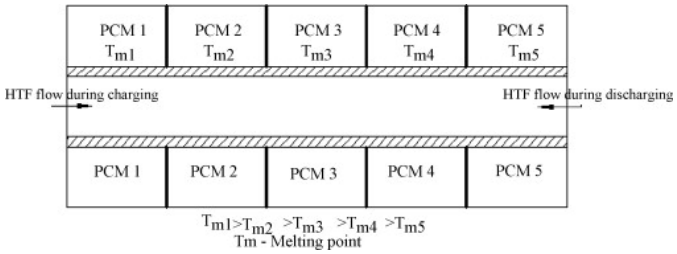

Figure 3.8.: *Multiple PCM's in a shell and tube latent heat TES [34]*

Thermal Conductivity Enhancement

The main disadvantage which limits the potential applications of latent heat TES is the low thermal conductivity of conventional PCMs. There are a few methods to increase the heat transfer in between HTF and PCM with increasing the thermal conductivity of the PCM by mixing in high conductivity additives [34]:

- Impregnation of high conductivity porous material with the PCM.
- Dispersion of high conductivity particles in the PCM.
- Placing of metal structures in the PCM.
- Use of high conductivity low density materials.

Impregnating porous structures made of aluminium, copper or graphite matrices with PCM can increase the effective thermal conductivity of the storage material significantly. The enhancement due to this method depends on both the thermal conductivity and the porosity of the matrix. Although low porosity matrices lead to a higher effective thermal conductivity, the effect of natural convection is reduced. According to studies from Mesalhy et al. [44] and Krishnan et al. [42] porous structures with high thermal conductivity and high porosity result in the highest possible enhancement. Probably the best choice to meet this requirements is expanded graphite. Due to the high absorbability of expanded graphite it enclosed the liquid PCM in its pores, forming a composite PCM with enhanced heat transfer properties. As states by Sari et al. [51] and Yin et al.

[62], melting and solidification times could be decreased by 65% and 26% respectively by using a composite PCM with a 5-10% expanded graphite mass fraction.

However composite PCM can only be prepared in time and energy consuming processes. A simpler solution would be to disperse small particles of high conductivity metals in the PCM in order to increase the effective thermal conductivity. Similar to the porosity of impregnated matrices is it as crucial to determine the optimum particle size as it is to minimize the heat transfer rate with minimum losses in storage capacity. Because of sedimentation and separation this method is only suitable for some types of PCM. Instead of dispersing small particles, the placement of metal structures in the PCM had been taken into account, with regards to heat transfer enhancement in latent heat TES. Velraj et al. [59] used hollow cylindrical steel structures which are submerged in the PCM in his research, reducing the time needed for solidification by a factor of 9. Anyhow, this improvement could only be reached with metal structures occupying 20% of the total storage volume.

Encapsulation

Another proposed way to increase the heat transfer rates in latent heat TES, is to increase the heat transfer surface, by embedding the PCM in small containers. These containers or shells can be of any size and structure. The shell-material has to be chosen in a way, that it stays solid and sealed over the whole operating temperature range. To manage the volume change of the PCM during the phase change an ullage space in the capsule is filled with e.g. air which can lead, due to the low thermal conductivity of air, to a bad performance. Depending on the size of the containers, two main technologies can be differentiated.

- **Makro-encapsulation** The encapsulation of a sodium nitrate/potassium nitrate mixture in tubular containers with an outer diameter of 75mm and a length of 77mm was investigated by Zhang et al. [64]. The disadvantages of this macro-encapsulation are the high manufacturing costs to maintain a hermetically sealed shell for the lifetime of the storage. In the work of Alam et al. [2] another technique for encapsulating PCMs is described. The PCM is pressed in spherical shapes and first coated by a polymer layer followed by a nickel plating, leading to a very thin and flexible but also strong encapsulation of the PCM.

- **Micro-encapsulation** Micro-encapsulation is an attractive way to improve the thermal performance of PCM by increasing the heat transfer surface with a better PCM/shell mass ratio than macro-encapsulation. The micro-encapsulation can either be accomplished by chemical or by mechanical processes. Zhang et al. [65] proposed a method to encapsulate a high temperature PCM (potassium nitrate) by coating it with a water limited silica coating. As stated by Jegadheeswaran et al. [34] this micro-encapsulation technology could also find use in improving the thermal performance of building materials, textile fabrics and thermal fluids.

4. Methods

4.1. Experimental Setup

The test rig used for the experimental investigations in this work, was constructed at the IET in 2018 for the usage in several previous research works (i.e. Urschitz et al. [52]). The construction of this test rig is based on experimental works of Prötsch [50] and Urschitz et al. [57] as well as numerical investigations of Walter et al. [60]. Prötsch examined a finned multi-tube heat exchanger in his work and concluded that a single tube system would make a better fit in order to determine the melting and solidification behaviour of the PCM in a latent heat TES. Therefore a single tube heat exchanger was constructed and investigated by Urschitz et al. ([57] and [52]). Urschitz found, that without transversal fins the liquid PCM accumulates at the top of the storage vessel during a melting process. This leads to a reduction of the active heat transfer surface and hence a bad performance of the test rig. To verify these experimental results, numeric investigations carried out by Walter et al. [60], conclude that a combination of arborescent longitudinal and transversal fins would be the best option in order to optimize the heat transfer behaviour in a latent heat TES of this type.

4.1.1. Thermal Oil Plant

To provide the latent heat test rig with the required heating and cooling power, it is connected to a thermal oil plant in which Therminol® VP-1 is utilized as heat transfer fluid. The thermal oil plant is divided into two sections, the primary circuit and the secondary circuit. In the primary circuit the thermal oil is pumped in a circle and heated by an electric heater with a maximum heating power of 280 kW_{th}. To prevent the thermal oil from evaporating when heated above 257 °C the primary circuit is equipped with an expansion vessel which can be pressurized with nitrogen. To reach temperatures of up to 400 °C the nitrogen pressure has to be increased up to approximately 11 bar. The utilized thermal oil has its crystallization point at 12 °C, which is why the whole plant is equipped with trace heating. The secondary circuit consists of the latent heat TES and a cooling system which is a combination of a 200 kW_{th} and a 5 kW_{th} water cooler. The two circuits are connected by a mixer which is controlled by the valve CV2.1. The whole plant is controlled and monitored by a process control system named APROL by B&R Industrial Automation GmbH. In Figure 4.1 a simplified process flow diagram of the thermal oil plant and the storage test rig is shown. Some important data of the thermal oil plant is summarized in Table 4.1.

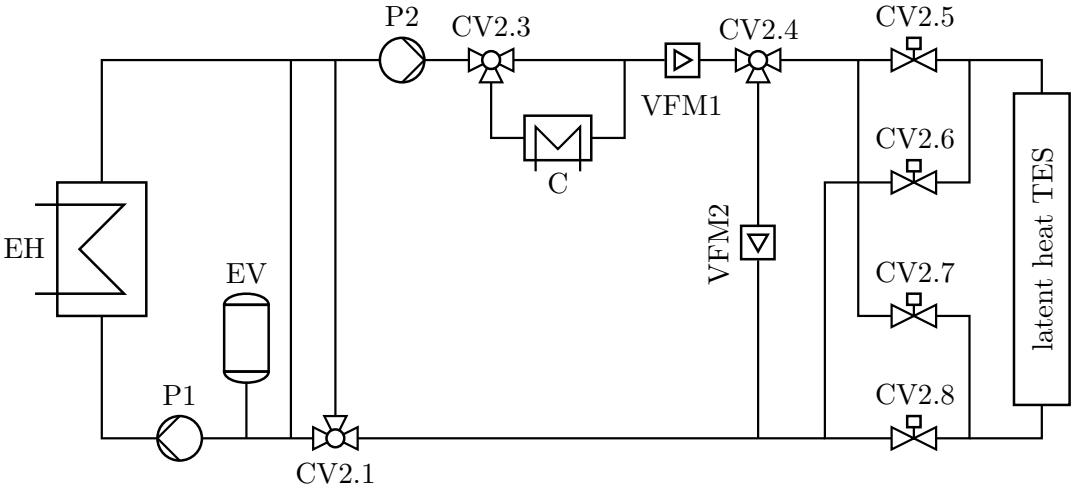

C ... 200kW water cooler
CV2.1 ... controlled valve for HTF temperature
CV2.3 ... controlled valve for HTF temperature
CV2.4 ... controlled valve for HTF mass flow
CV2.5-2.8 ... controlled valves for HTF flow direction
EH ... 280kW electric heater
EV ... nitrogen pressurized expansion vessel
P1 ... primary circuit pump
P2 ... secondary curcuit pump
VFM1&2 ... vortex flow meter

Figure 4.1.: *Process flow diagram of the experimental setup*

Table 4.1.: *Summary of parameters: thermal oil plant*

Thermal oil plant	
Heat transfer fluid	Therminol® VP-1 [1]
max. heating power	280 kW_{th}
max. cooling power	205 kW_{th}
Temperature sensors	PT100
Mass flow sensors	Proline Prowirl 72 vortex flow meter
max. mass flow	$3\,kg\,s^{-1}$
Mass flow for experiments	$1\,kg\,s^{-1}$
Flow temperature (charging phase)	336 °C (30 °C above melt. temp. of PCM)
Flow temperature (discharging phase)	276 °C (30 °C below melt. temp. of PCM)

4.1.2. Test Rig (Latent Heat TES)

The experimental setup consists of a vertically arranged shell-and-tube heat exchanger. The HTF is flowing through the inner steel tube on which longitudinal aluminium fins are mounted for heat transfer enhancement. The volume between the inner- and the outer tube is filled with the storage material, which in this case is a phase change material. To minimize heat losses to the surrounding, the TES is insulated with a 250 mm layer of stone wool. In addition to the longitudinal fins, 5 transversal fins were added in order to prevent the liquid PCM from accumulating at the top of the storage vessel.

The storage vessel as well as the HTF-containing tube are made of P235GH pressure vessel steel, the fins consist of extrusion molded aluminium EN-AW6060. Except for the HTF-containing steel tube, the whole test rig (meaning the storage system) is designed for temperatures of up to 400 °C and atmospheric pressures. For the HTF to reach temperatures of more than 257 °C it has to be pressurized and hence all HTF-containing parts are designed for a nominal pressure of 16 bar and a temperature of 400 °C. For the research in this work the flow direction of the HTF is set from bottom to top which should not have any impact on the results, as found in a previous publication of Urschitz et.al. [57]. In Figure 4.2 some photos of the uninsulated TES and the heat exchanger tube equipped with the fins are presented. A summary of the most important data of the latent heat TES is presented in Table 4.2.

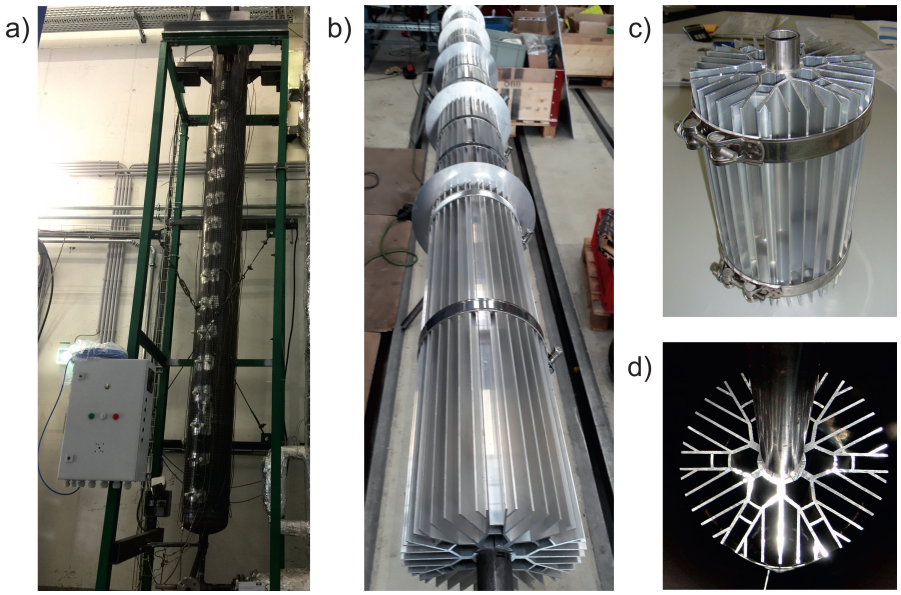

Figure 4.2.: *a) uninsulated test rig of the latent heat TES b) combination of longitudinal and transversal fins c) and d) fins fixed with hinge bolt clamps*

Table 4.2.: *Summary of parameters: latent heat TES & and fins*

Latent heat TES and fins	
Storage type	Vertical shell-and-tube heat exchanger
Heat transfer enhancement	Combination of arborescent longitudinal and transversal fins
Fin material	Aluminium EN-AW6060
Number of finned tubes	1
Number of transversal fins	5
Volume fractions	82.5 % PCM, 14.7 % Aluminum, 0.87 % Steel, 1.93 % HTF
Temperature sensors	PT100
Operating temperature range	±30 °C around the melting point of PCM
Storage capacity	7.91 kW h
Mean charging power rate	6.78 kW
Mean discharging power rate	−5.72 kW
Nominal energy density	110.41 kW h m^{-3}
Net energy density	98.00 kW h m^{-3}

4.1.3. Heat Transfer Enhancement

As already mentioned, a combination of arborescent longitudinal and transversal fins is utilized as heat transfer enhancement in the examined latent heat TES. This combination was chosen based on the findings of Urschitz et al. [57] and Walter et al. [60]. In Figure 4.3 the fin geometry with some important dimensions is illustrated.

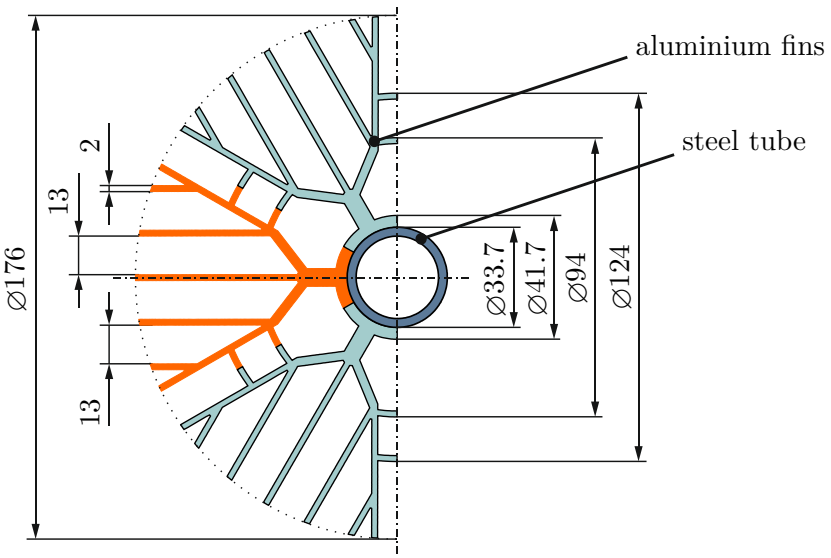

Figure 4.3.: *Fin geometry*

The fins consist of extrusion molded Aluminium EN-AW6060 segments which are mounted on the steel tube. The shape of such a segment is highlighted (orange) in Figure 4.3. The fins are designed in a way, that the maximum gap between two aluminium-surfaces is 13 mm. In order to compensate the differences in thermal expansion coefficients of steel and aluminium hinge bolt clamps are used to attach the aluminium fins to the steel tube. A similar experimental setup was investigated by Urschitz et al. [57] back in 2014. Based on their findings 5 evenly spaced transversal fins are added in order to prevent the liquid PCM to accumulate at the top of the storage during the melting process. These transversal fins vertically seperate the storage tank into 5 chambers. Each chamber has a height of 600 mm (neglecting the thickness of the transversal fins), which leads to an overall storage height of 3 m.

4.1.4. Storage Material

Sodium nitrate ($NaNO_3$) is utilized as storage material. The melting point of sodium nitrate (306 °C) matches flow temperatures of parabolic through CSP plants, and it could be used to store heat to supply steam cycles with live steam properties of e.g. 275 °C and 60 bar. Sodium nitrate is an inorganic, crystalline salt with a molar mass of 84.99 $g\,mol^{-1}$. At room temperature it is solid and has a white/colorless appearance. It is hygroscopic and soluble in water but doesn't form stable salt hydrates in the solid state. In its solid form sodium nitrate finds use in industries like fertilizer-, glas- or explosives production. Molten sodium nitrate is currently used in form of a mixture with other salts for heat treatment of metals or as a heat transfer fluid and storage medium in modern CSP-plants.

According to long term tests from Bauer et al. [6] sodium nitrate is thermally stable for temperatures below 350 °C and only little decomposition to sodium nitrite can be recognized for temperatures below 450 °C. At temperatures above 450 °C a significant amount of sodium nitrate decomposes to sodium nitrite which results in a decrease of the melting temperatures and a lower enthalpy of fusion. When sodium nitrate is heated to temperatures above 550 °C it undergoes further decomposition by releasing nitrogen oxides. Therefore the area of application for sodium nitrate as a storage material is limited to temperatures below 450 °C. Since the operating temperature range for the experiments carried out is chosen between 276 °C and 336 °C the nitrite formation and decomposition of sodium nitrate will have no impact on the results. Some interesting data of sodium nitrate is summarized in Table 4.3.

Thermophysical Properties of Sodium Nitrate

The most important thermophysical properties of a storage material utilized in a latent heat TES are density, specific heat capacity and thermal conductivity. Together with the specific heat capacity, the mass-density of a PCM defines the volume based storage density which is an important parameter for the design of thermal energy storage systems. Further the density should remain high for the whole operating temperature range

Table 4.3.: *Summary of parameters: storage material*

Storage material	
PCM type	Sodium nitrate, $NaNO_3$
Melting temperature	306 °C [6]
Density at 306 °C liquid	1.908 kg dm^{-3} [6]
Enthalpy of fusion	178 kJ kg^{-1} [6]
Mass in section 1/2/3, (see Sec. 4.1.5)	17.90 kg m^{-1}/18.77 kg m^{-1}/25.37 kg m^{-1}

of the storage in order to simplify the construction of the storage vessel. The density of sodium nitrate at 25 °C is 2260 kg m^{-3} and decreases slightly with rising temperature. At the melting point the density exhibits a finite discontinuous drop of about 10% which, compared to the thermal expansion in the solid and liquid state, is the crutial value for the design of the storage tank.

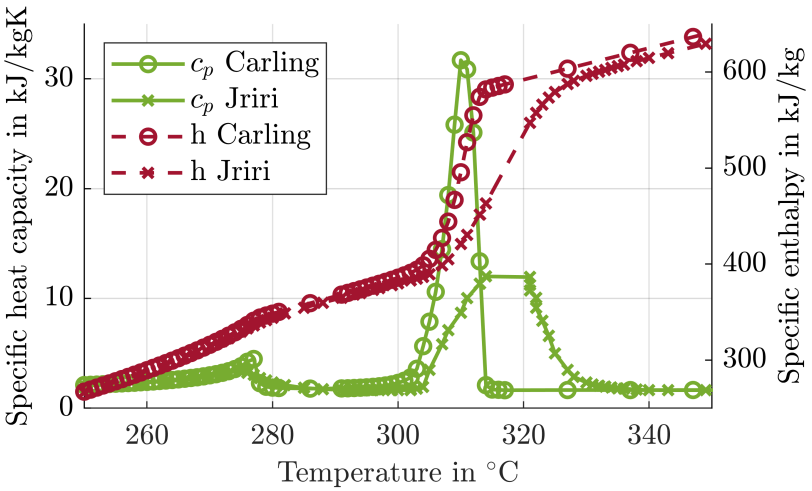

Figure 4.4.: *Specific heat capacity and specific enthalpy of sodium nitrate, data from [10] and [40]*

Detailed investigations on the specific heat capacity and the latent heat of fusion are provided by Carling et al. [10] and Jriri et al. [40]. The data collected in these papers is shown in Figure 4.4. Based on that a melting temperature of 306 °C and a latent heat of fusion of 178 kJ kg^{-1} is used for the analysis in this work. As can be seen in Figure 4.4 a second order (solid/solid) phase transition is present at temperatures around 275°C. For the latent heat of this phase transition values between 12 kJ kg^{-1} and 45 kJ kg^{-1} are reported. The exact implementation of the data collected by Carling and Jriri for data analysis is presented in Section 4.3.1.

Another substantial parameter for the design of a latent heat TES is the thermal

conductivity of the storage material. For sodium nitrate in the liquid phase values around 0.6 $\mathrm{W\,m^{-1}\,K^{-1}}$ are reported by several authors like Bauer et al. [6]. For the solid phase no reliable values could be found. Based on previous experiments with latent heat TES the thermal conductivity of a PCM in the solid state seems to be similar to the liquid state, or even a bit higher.

4.1.5. Measurement Methods and Sensor Placement

For the data analysis the storage volume is radially discretized into 4 sections in a way that every section represents the same mass of PCM. A cross section of the storage and the discretization is shown in Figure 4.5. The outer section, section 4 is not shown in this picture, because only the data measured in the sections 1 to 3 is used for data analysis. The temperature in section 4 is needed to recognize stationary cycling of the TES (when the temperature in section 4 remains constant for a certain number of cycles, the TES is said to be stationary). The test rig is equipped with 40 PT100 temperature sensors. 15 sensors in section 1 and 2 each, 4 sensors in section 3 and 4 each, one for the HTF-inlet and one for the HTF-outlet. The sensors in each section are evenly spaced, their angular and radial positions are shown in Figure 4.5. As found in previous investigations from Scharinger-Urschitz [52], thanks to the transversal fins, the melting and solidification behaviour of the PCM in the examined latent heat TES is axially symmetric. Therefore the representative temperature for each section is calculated by an arithmetic average for all the sensors in each section.

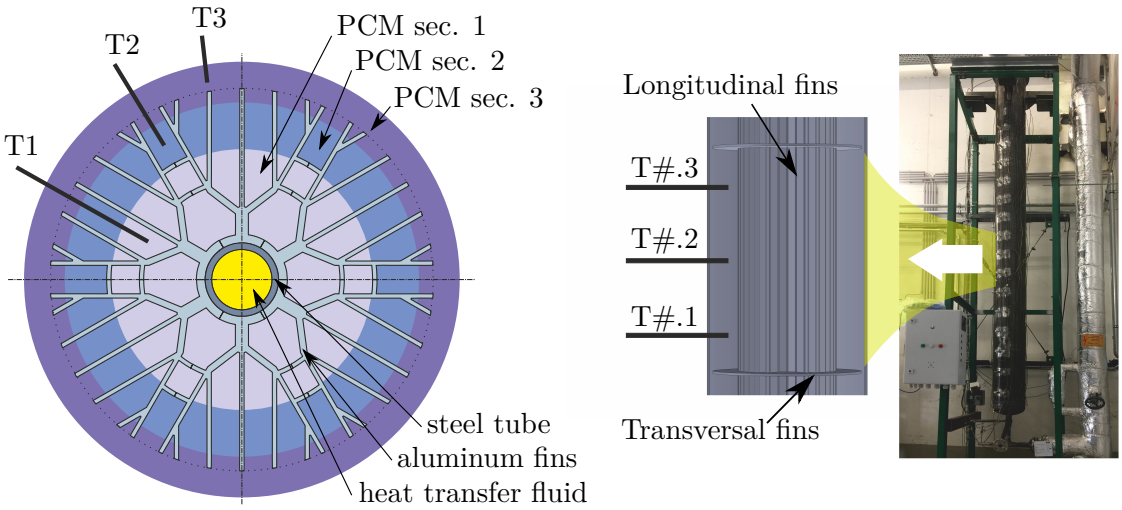

Figure 4.5.: *Storage cross section and discretization of the storage volume incl. radial and vertical position of the temperature sensors and a picture of the non-insulated test rig*

For the mass flow measurement of the HTF, two Proline Prowirl 72 vortex flow meter sensors are utilized as it can be seen in Figure 4.1. The thermal oil plant is designed in a way, that the oil pumps always transport the maximum oil mass flow. The thermal oil mass flow to the consumer (in this case a latent heat TES) is controlled by a bypass-valve (CV2.4 in Figure 4.1). One vortex sensor is placed before the bypass-valve and the other one in its bypass, which means, that the thermal oil mass flow to the consumer isn't directly measured but indirectly by subtracting the values of both measurements. This setup was chosen in order to be able to measure mass flows which are below the lower limit of the validity range of the sensors.

4.2. Experimental Control – Partial Cycle Operation Modes

For the evaluation of the partial cycling behaviour of a latent heat TES the term "state of charge" (SOC) is used to quantify the energy stored in the TES. The SOC is 0 for a fully discharged, 1 for a fully charged and in between for a partially charged TES. It represents the ratio of the stored energy to the maximum storable energy. The definition of the SOC is presented in Section 4.3 in more detail. For the experiments the SOC is continuously calculated by the process control system based on temperature measurements in the PCM. This allows the examined TES to operate SOC-controlled. Basically two types of experiments can be differentiated:

- Starting from $SOC = 0$: The initial state is a fully discharged storage ($SOC = 0$). The storage is partially charged ($0 < SOC < 1$) and discharged until $SOC = 0$ is reached again.
- Starting from $SOC = 1$: The initial state is a fully charged storage ($SOC = 1$). The storage is partially discharged ($0 < SOC < 1$) and charged until $SOC = 1$ is reached again.

The goal of this experiments is to evaluate the impact of partially charging/discharging a latent heat TES on the following discharging/charging process. The flow temperature of the HTF is set to 336 °C for a charging phase and to 276 °C for a discharging phase, which is 30 °C above/below the melting temperature of sodium nitrate respectively.

4.3. State of Charge Formulation

The amount of stored energy is an essential parameter for the characterization of energy storage systems in general. The ratio of stored energy to the total amount of storable energy is called ratio of accumulated energy in [23] or ratio of energy [4]. The term "state of charge" appeared more suitable and refers to definitions in [5]. Slight differences may appear due to the inclusion of the sensible heat within the melting range. Compared to the latent heat of fusion the inclusion of the sensible heat won't have a significant impact on the resulting formulation, but this seems to be a more realistic approach. A classification of available techniques for the determination of the SOC including expe-

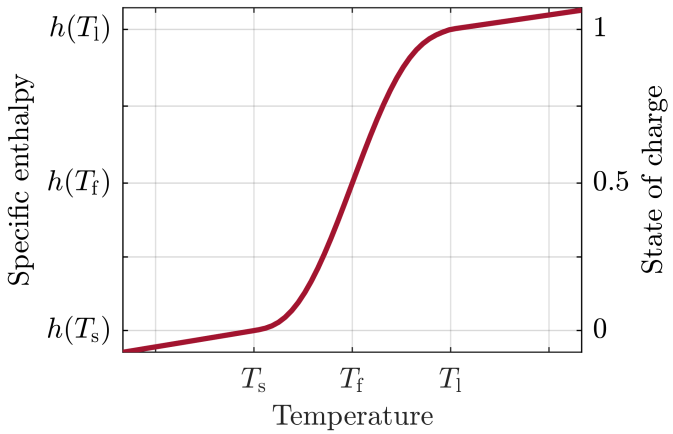

Figure 4.6.: *SOC formulation*

rimantal analysis is provided by Zsembinszki et al. [68]. Due to isobaric conditions in the TES the *SOC* can be calculated with enthalpy differences as it can be seen in Eq. (4.1). The function for the specific enthalpy in dependence of the temperature ($h(T)$) is derived in Section 4.3.1.

$$SOC\,(T) = \frac{\bar{h}\,(T) - h\,(T_\mathrm{s})}{h\,(T_\mathrm{l}) - h\,(T_\mathrm{s})} \tag{4.1}$$

With this formulation (Eq. (4.1)) the *SOC* is 0 at $T = T_\mathrm{s}$ and 1 at $T = T_\mathrm{l}$. The denominator represents the specific energy which can be stored in the PCM when heating from the solidification temperature T_s to the liquefaction temperature T_l. The average specific enthalpy $\bar{h}\,(T)$ of the storage material is calculated as a weighted arithmetic mean over the three sections displayed in Figure 4.5.

$$\bar{h}\,(T) = \frac{\sum_{i=1}^{3} m_i\, h\,(T_i)}{\sum_{i=1}^{3} m_i} \tag{4.2}$$

In Eq. (4.2) m_i represents the mass of PCM in section i and $h\,(T_i)$ the specific enthalpy at the averaged temperature T_i of the PCM in section i. The exact values of m_i are given in Table 4.3. In Figure 4.6 the correlation between the specific enthalpy of the storage material $h\,(T)$ and the *SOC* can be seen.

The *SOC* definition in Eq. (4.1) is only applicable when the storage is cycled exactly across the melting range, which is fine for the investigations carried out in this study. Nevertheless, in real applications the storage will also be operated above and below that range. The enthalpy distribution function derived in Eq. (4.8) is valid for temperatures between 100 °C and 400 °C. Therefore the formulation of the *SOC* can be expanded to a

wider temperature range by replacing T_s and T_l in Eq. (4.1) with the new temperatures that should be associated with $SOC = 0$ and $SOC = 1$ respectively.

In all mentioned references including the present formulation, the SOC formulation is storage-temperature dependent. At the melting point, theoretically the temperature in the storage remains at the melting temperature. With a temperature depended SOC formulation, the SOC would not be steady. In praxis, the temperatures in the discretized regions are not homogeneous. The challenges coming along with this assumption will be discussed in Section 5.

4.3.1. Enthalpy of Fusion Distribution Function

To calculate the state of charge based on temperature measurements in the PCM, a function for the specific enthalpy depending on the temperature has to be developed. For pure substances, a first order phase transition is accompanied by discontinuous changes of the extensive state variables in theory. Eq. (4.3) shows a function for the specific enthalpy of a PCM which satisfies this behavior.

$$h\left(T\right) = h_\mathrm{sens}\left(T\right) + L\,H(T - T_\mathrm{f}) \tag{4.3}$$

The Heaviside step function $H(T - T_\mathrm{f})$ shown in Eq. (4.3) can be applied to mathematically formulate an isothermal phase change. However, such a sharp phase transition will only occur in a system with an infinitesimal volume or with a PCM with an infinite thermal conductivity. Since none of these two requirements apply to the test rig examined in this work, the enthalpy of fusion is distributed over a characteristic melting range. Due to this distribution, an apparent specific heat capacity of the PCM is calculated as it can be seen in Eq. (4.4).

$$c_\mathrm{app}\left(T\right) = \begin{cases} c_\mathrm{s}\left(T\right), & T_\mathrm{lrv} \leq T < T_\mathrm{s} \\ c_\mathrm{m}\left(T\right) + c^*\left(T\right), & T_\mathrm{s} \leq T \leq T_l \\ c_\mathrm{l}\left(T\right), & T_\mathrm{l} < T \leq T_\mathrm{urv} \end{cases} \tag{4.4}$$

The apparent specific heat capacity c_app can be written in the form given in Eq. (4.4) consisting of a function c_s for the solid area (below T_s), a function c_l for the liquid area (above T_l) and a combination of a linear function c_m and a fourth degree polynomial function c^* in the melting range (between T_s and T_l). The function c_m represents the sensible part of the specific heat in the melting range and is calculated by a simple linear interpolation between $c_s\left(T_s\right)$ and $c_l\left(T_l\right)$. The validity of the functions is limited to the lower range temperature (T_{lrv}) and the upper range temperature (T_{urv}).

$$L = \int_{T_\mathrm{s}}^{T_\mathrm{l}} c^*\left(T\right)\mathrm{dT} \tag{4.5}$$

To distribute the enthalpy of fusion over the melting range, the fourth degree polynomial function is designed in a way, that its integral from T_s to T_l equals to the enthalpy of fusion, as described in Eq. (4.5). When fitting the functions just mentioned to the data for sodium nitrate measured by Jriri et al. [40], the specific heat capacity can be

formulated by 3 seperate polynomial functions as it is shown in Eq. (4.6).

$$c_{\mathrm{app}}(T) = \begin{cases} \sum_{n=0}^{1} a_n T^n, & T_{\mathrm{lrv}} \leq T < T_{\mathrm{s}} \\ \sum_{n=0}^{4} b_n T^n, & T_{\mathrm{s}} \leq T \leq T_l \\ c_0, & T_{\mathrm{l}} < T \leq T_{\mathrm{urv}} \end{cases} \tag{4.6}$$

The parameters for each area are given in Table 4.4.

Table 4.4.: *Parameters for the polynomial functions [52]*

n	0	1	2	3	4
a_n	0.9262	0.003214	0	0	0
b_n	-791.55	0.0032	3.1444	-0.5247	0.0219
c_n	1.65	0	0	0	0

Further, the function for the specific enthalpy is calculated by integrating Eq. (4.4) including the enthalpy at the reference temperature T_0, h_0.

$$h(T) = \int_0^T c_{\mathrm{app}}(T)\,\mathrm{dT} + h_0 \tag{4.7}$$

Integration of Eq. (4.7) for sodium nitrate leads to Eq. (4.8).

$$h(T) = \begin{cases} \sum_{n=0}^{1} \frac{a_n}{n+1} T^{n+1}, & T_{\mathrm{lrv}} \leq T < T_{\mathrm{s}} \\ \sum_{n=0}^{4} \left(\frac{b_n}{n+1} T^{n+1} \right) - 422.14, & T_{\mathrm{s}} \leq T \leq T_{\mathrm{l}} \\ c_0\, T + 135.19, & T_{\mathrm{l}} < T \leq T_{\mathrm{urv}} \end{cases} \tag{4.8}$$

The distribution of the latent heat over a specific temperature range enables differentiable and steady enthalpy formulations. The selection of the suitable temperature range between T_{s} and T_{l} has to be done by iteration and mainly depends on the discretization of the storage. For the experiments which were carried out in the course of this work, the solidification temperature T_{s} was set to 300 °C and the liquefaction temperature T_{l} to 312 °C. The resulting trends of the apparent specific heat and the specific enthalpy as well as the separate functions for the sensible and latent part are shown in Figure 4.7.

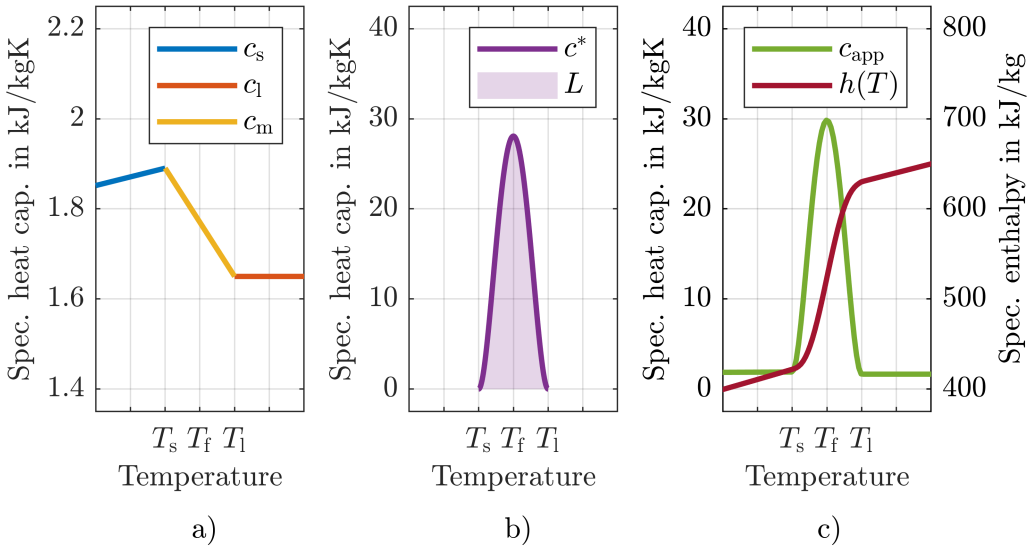

Figure 4.7.: *a) Sensible part of the specific heat capacity b) Latent part of the specific heat capacity c) Apparent specific heat capacity and specific enthalpy*

4.4. Data Analysis

In order to make a statement about the partial load behaviour of latent heat TES, the data collected are used to calculate the power rate of the storage.

$$P_{\mathrm{HTF}} = \dot{m}_{\mathrm{HTF}} \left(h_{\mathrm{in}} - h_{\mathrm{out}}\right) \tag{4.9}$$

As can be seen in Eq. (4.9) the power rate is calculated by applying the first law of thermodynamics to the HTF-stream. Which means, that this power rate also includes the losses.

To validate the measured data, the energy balance for the storage is calculated by applying the first law of thermodynamics to the whole storage as it is shown in Eq. (4.10).

$$U_{\mathrm{TES}}\left(t\right) - U_{\mathrm{TES}}\left(0\right) = \int_0^{\mathrm{t}} P_{\mathrm{HTF}}\left(t\right) \mathrm{dt} - \int_0^{\mathrm{t}} P_{\mathrm{loss}}\left(t\right) \mathrm{dt} \tag{4.10}$$

The left side of Eq. (4.10) represents the stored energy for a certain operation time t of the storage. The right side includes the energy input by the HTF and the losses for the operation time t.

With the measured temperature data and Eq. (4.8), the left part of the energy balance expands to

$$\underbrace{\sum_{i=1}^{3} m_{\mathrm{Alu},i}\, c_{\mathrm{Alu}}\, \left(T_i\left(t\right) - T_i\left(0\right)\right)}_{\text{Energy stored in the aluminium fins}} + \underbrace{\sum_{i=1}^{3} m_{\mathrm{PCM},i}\, \left(h_i\left(t\right) - h_i\left(0\right)\right)}_{\text{Energy stored in the PCM}} . \tag{4.11}$$

The stored energy is calculated for aluminum and PCM only, steel parts and insulation are neglectable due to their little mass and low heat capacity. The losses had been determined in previous investigations and are temperature dependent between 350 W and 440 W for 276 °C and 336 °C respectively. A linear function is applied for the losses.

4.4.1. Estimation of Measurement Errors

To estimate the impact of the uncertainties of the measured data on the calculated power rate, the Gaussian law of error propagation is applied to Eq. (4.9), which leads to Eq. (4.12).

$$\delta P^2 = \left(\frac{\partial P}{\partial \dot{m}}\right)^2_{\hat{\mathrm{h}}_{\mathrm{in}},\hat{\mathrm{h}}_{\mathrm{out}}} \delta\dot{m}^2 + \left(\frac{\partial P}{\partial h_{\mathrm{in}}}\right)^2_{\hat{\mathrm{m}},\hat{\mathrm{h}}_{\mathrm{out}}} \delta h_{\mathrm{in}}^2 + \left(\frac{\partial P}{\partial h_{\mathrm{out}}}\right)^2_{\hat{\mathrm{m}},\hat{\mathrm{h}}_{\mathrm{in}}} \delta h_{\mathrm{out}}^2 \tag{4.12}$$

$$\delta h_i = c_p\left(T_i\right)\, \delta T_i \tag{4.13}$$

The temperature sensors in the HTF had been calibrated in order to minimize the error. After calibration, the accuracy of the calibrated sensors is about ±0.1 K at operation temperature. This leads to a measurement error based on Eq. (4.12) of ±0.343 kW. This measurement error has no significant influence on the results.

5. Results and Discussion

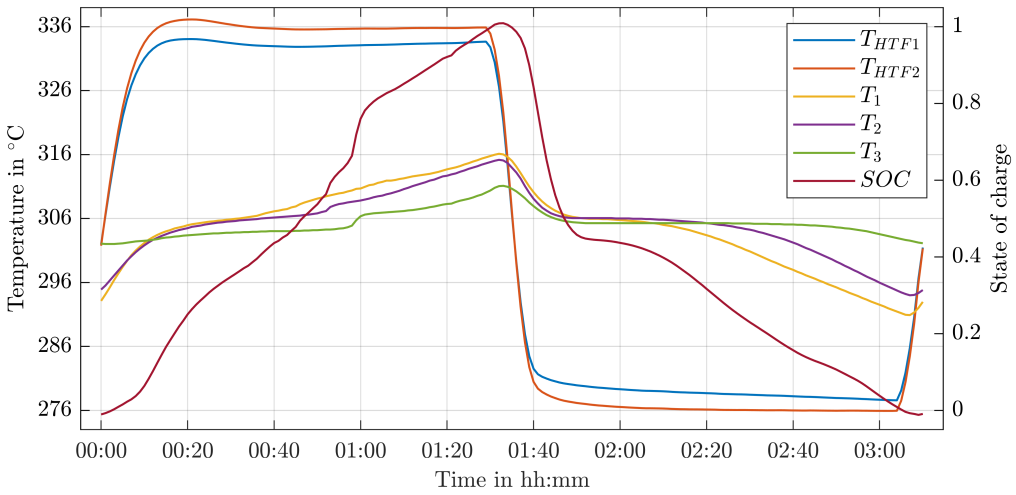

Figure 5.1.: *Temperature and SOC trend for the full cycle*

In Figure 5.1 a representative data set for a full load cycle is shown. T_{HTF2} and T_{HTF1} represent the inlet and outlet temperature of the thermal oil, controlled by the thermal oil plant. The thermal oil mass flow was set to a constant value of 1 $\mathrm{kg\,s^{-1}}$. T_1, T_2 and T_3 represent the averaged temperatures of the PCM for each radial section. The presented data set starts at $SOC = 0$ and ends at $SOC = 0$. At the beginning both the inlet and outlet temperature of the HTF are approximately 306°C, which means that the power rate is zero as well. As the HTF flow temperature rises to the preset charging value (336°C) the temperature of the PCM follows until $SOC = 1$ is reached. At this point the thermal oil plant is switched to cooling mode and the HTF flow temperature drops to the preset discharging value of 276°C. This switching period takes 15-20 minutes, which has to be taken into account when considering the results presented in Figure 5.2 and 5.3. As soon as $SOC = 0$ is reached, the thermal oil plant is switched to heating mode and the whole cycle starts all over again. Due to heat losses in the thermal oil plant the switching period from cooling to heating mode takes slightly longer than switching from heating to cooling mode.

When taking the fundamentally different heat transfer mechanisms for charging and discharging into account, one might think that the times required for charging and discharging a latent heat TES have to be significantly different. This is what also has been reported in comparable investigations like the one from Gasia et al. [23].

In any case, the data presented in Figure 5.1 show different results. The times taken for charging and discharging the storage are equal, which means that the dominant heat transfer mechanism in the examined storage is the heat conduction in the aluminium fins. Hence it can be stated, that the utilized combination of arborescent longitudinal and transversal fins is suitable for heat transfer enhancement in high temperature latent heat TES.

The trends of the temperature measurements in Figure 5.1 clearly show the expected phase change plateau for the discharging process. Immediately after switching the thermal oil plant to cooling mode, the temperature at every testing point in the PCM drops down to the melting temperature (306°C). This is probably caused by the natural convection in the liquid PCM, heat losses to the surrounding and the thermal inertia of the whole system. In contrast, the temperature trends exhibit pretty constant slopes for a charging process. That's why the SOC formulation very well correlates to the actual storage capacity during charging. Due to the stable temperature plateau at the melting temperature - especially while discharging - the temperature based enthalpy distribution leads to a non uniform SOC gradient for discharging. Referring to Figure 5.1, the flow temperature of the HTF reaches the preset discharging value (276°C) at about 02:00 (x-axis value). At this time the SOC already dropped down to a value of approximately 45%. The impact of this disadvantage on the results is discussed in the following sections, Section 5.1 and 5.2, in more detail. Additional temperature trends of the partial cycle experiments are provided in Appendix A.1.

5.1. Power Rates

In Figure 5.2 and 5.3 the power rates in dependence of the SOC are shown for different partial and full cycle operation modes. Figure 5.2 presents the full cycle and all partial cycles starting from $SOC = 0$. The full load cycle and all partial cycles starting from $SOC = 1$ are shown in Figure 5.3. The mean power rate for charging is 6.78 kW with a 95.45 % confidence interval of ±1.14 kW for all cycles. The mean discharging power rate is −5.72 kW with a 95.45 % confidence interval of ±1.36 kW for all cycles. In the diagrams the power rate is normalized with the mean charging power rate of 6.78 kW, which is also referred to as the nominal power rate. The lowest power rates measured for the charging and discharging processes were 76% and 56% of the nominal power rate respectively. These low values are caused by a narrow volume, which is not penetrated by fins, near the perimeter of the cylindrical heat exchanger. This is why they should not be taken too seriously when evaluating the efficiency of the fins.

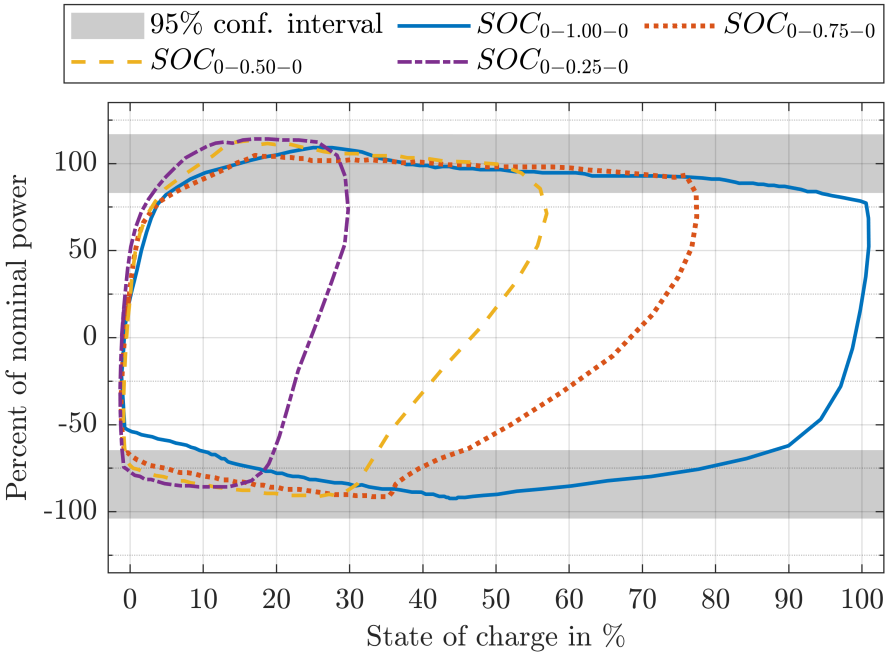

Figure 5.2.: *Power rates for different SOC cycles starting from* $SOC = 0$

The impact of the non uniform SOC gradient for discharging on the results can nicely be explained by the yellow ($SOC_{0-0.50-0}$) loop in Figure 5.2. This cycle starts at $SOC = 0$ (the whole PCM is solid) with a power rate of 0. After switching the thermal oil plant to heating mode the power rate rises until the thermal oil reaches the preset flow temperature. During this heating period the SOC already reaches a value of

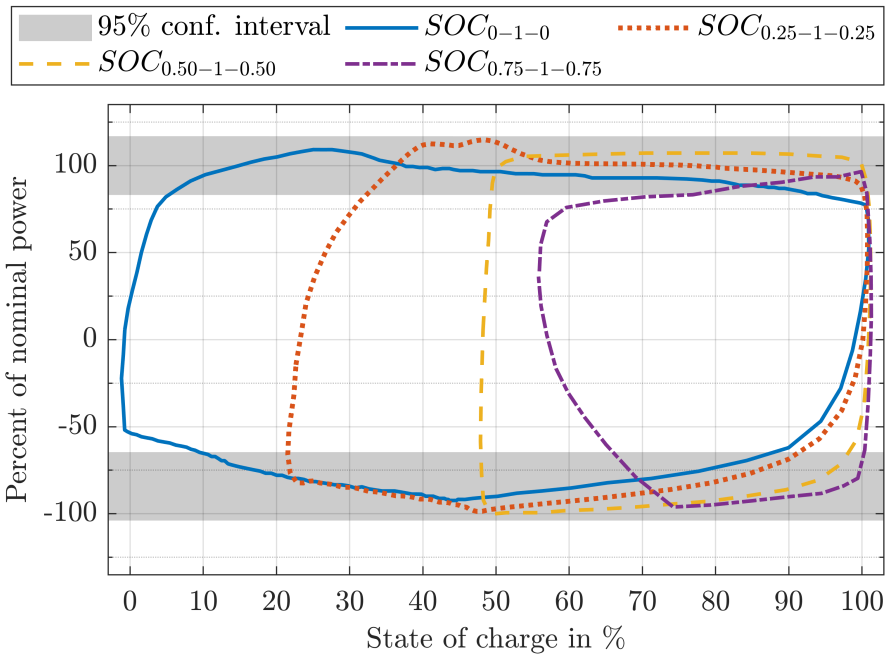

Figure 5.3.: *Power rates for different SOC cycles starting from* $SOC = 1$

about 10%. When reaching $SOC = 0.5$ the thermal oil plant switches to cooling mode and the power rate starts to decline. During this switching period, which takes about 15-20 minutes, the temperatures in the TES equalize, leading to a declining SOC even though the power rate is still positive. That is why the power rates during a switching period of the thermal oil plant operation mode aren't representative and therefore aren't taken into account for the determination of the mean power rates and their confidence intervalls.

Overall, the results presented in this section are very promising for further development of latent heat TES. Thanks to the novel fin design a nearly constant power rate for all operation modes is reached. Compared to previous investigations where the power rate for discharging is an order of magnitude lower at the end of discharging (e.g. [23]), the heat transfer enhancement with a combination of longitudinal and transversal fins is remarkable.

5.2. Energy Balance

In order to validate the measured data and for valuation of the *SOC* formulation an energy balance was calculated for the storage tank and is visualized in Figure 5.4. In Figure 5.4 the PCM based energy is plotted against the HTF based energy for a) charging and b) discharging. The deviation of the graphs is caused by losses and the inaccuracies in the *SOC* formulation. Eq. (4.11) is used to calculate the PCM based energy, while the HTF based energy is calculated by integrating Eq. (4.9) over the operating time. The red lines indicate the full cycle $SOC_{0.00-1.00-0.00}$, the blue lines the partial cycles.

For charging (Figure 5.4a) both sides of the energy balance reveal similar values leading to a nearly constant slope of the trends. Different results are shown in Figure 5.4b for the discharging process. Caused by the temperature plateau during discharging the PCM- and HTF based energies show high deviations around the melting temperature.

In summary it can be said that the *SOC* formulation developed in the work is only applicable for charging processes. For the characterization of a latent heat TES during a discharging process another strategy has to be chosen. Such a strategy can either be based on a different measuring method (pressure- or density measurement instead of temperature measurement) or a more complex enthalpy distribution function than the one developed in this work.

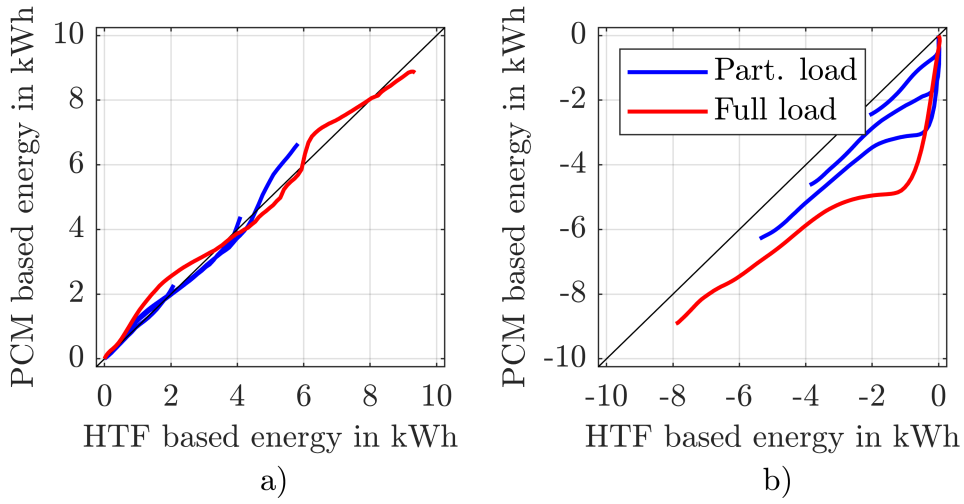

Figure 5.4.: *Energy balance for a) charging phases, starting at SOC_0 and b) discharging phases, ending at SOC_0*

6. Conclusion and Outlook

A high temperature latent heat thermal energy storage is subject of the experimental investigations in this work. The examined storage consists of a single shell and tube heat exchanger with arborescent longitudinal and transversal fins for heat transfer enhancement. Sodium nitrate with a melting temperature of 306°C is utilized as storage material. The latent heat of fusion of sodium nitrate is 178 $\mathrm{kJ\,kg^{-1}}$ which leads to a nominal storage capacity of 7.91 kW h. The storage tank is equipped with two temperature measurement points and a mass flow measurement in the heat transfer fluid stream and 38 temperature measurement points in the phase change material. The storage volume is discretized in 4 radial sections in a way that every section contains a similar mass of sodium nitrate and aluminium. For data analysis a distribution function for the latent heat of fusion to a certain melting range and a mathematical formulation of the state of charge are developed.

The goal of the experiments carried out is to evaluate how the state of charge influences the power rates of a charging/discharging process for different partial cycle operation modes. The examined data show very promising results in terms of high power rates for every state of charge and all partial cycle operation modes. A mean charging power rate of 6.78 kW with a 95.45 % confidence interval of ± 1.14 kW and a mean discharging power rate of -5.72 kW with a 95.45 % confidence interval of ± 1.36 kW is determined. Therefore it can be stated that with the utilized combination of longitudinal and transversal fins the state of charge does not have any impact on the power rate of latent heat storage systems. The minimum charging/discharging power rate is as high as 83% or 76% of the mean charging/discharging power rate respectively and not dependent on the state of charge or the partial cycle operation modes. These values are highly promising for further development and application of latent heat thermal energy storage systems.

Further investigations may concentrate on alternative state of charge formulations and enthalpy distribution functions. As discussed in the results section the state of charge formulation doesn't really correlate for a discharging process. This problem is caused by the fundamentally different heat transfer mechanisms which are dominant during a charging (melting) and a discharging (solidification) process. For a melting process in the examined storage type the chosen melting point (306 °C) and melting range (300 °C - 312 °C) lead to a very well correlating enthalpy distribution function. Due to the rapid temperature drop at the beginning of a solidification process the melting point needs to be lower and the melting range significantly smaller. Therefore two separate enthalpy distribution functions for each charging and discharging may be a suitable solution for this problem.

Unlike the test rig examined in this work, a utility scale latent heat thermal energy storage will consist of multiple heat exchanger tubes which can be connected in series or parallel. To achieve the maximum power rate, the temperature difference between the hot and the cold side of a heat exchanger needs to be maximized. Therefore a series connection of the heat exchanger tubes is not suitable for a latent heat thermal energy storage. For a parallel connection of the tubes the heat transfer fluid mass flow will split up, which lowers the flow velocity of the heat transfer fluid, leading to a declining heat transfer coefficient on the inside of the heat exchanger tubes. Future investigations may therefore focus on the critical velocity at which the heat transfer coefficient at the inside of the tube becomes the bottleneck of the overall heat transfer rate.

References

[1] Solutia Europe S. A. *Datasheet Therminol VP1: Vapour Phase Liquid Phase Heat Transfer Fluid 12°C to 400°C*.

[2] Tanvir E. Alam et al. "Macroencapsulation and characterization of phase change materials for latent heat thermal energy storage systems". In: *Applied Energy* 154 (2015), pp. 92–101. ISSN: 03062619. DOI: 10.1016/j.apenergy.2015.04.086.

[3] Guruprasad Alva, Yaxue Lin, and Guiyin Fang. "An overview of thermal energy storage systems". In: *Energy* 144 (2018), pp. 341–378. ISSN: 03605442. DOI: 10.1016/j.energy.2017.12.037.

[4] Simone Arena et al. "Numerical analysis of a latent heat thermal energy storage system under partial load operating conditions". In: *Renewable Energy* 128 (2018), pp. 350–361. ISSN: 09601481. DOI: 10.1016/j.renene.2018.05.072.

[5] Tilman Barz et al. "State and state of charge estimation for a latent heat storage". In: *Control Engineering Practice* 72 (2018), pp. 151–166. ISSN: 09670661. DOI: 10.1016/j.conengprac.2017.11.006.

[6] Thomas Bauer, Doerte Laing, and Rainer Tamme. "Characterization of Sodium Nitrate as Phase Change Material". In: *International Journal of Thermophysics* 33.1 (2012), pp. 91–104. DOI: 10.1007/s10765-011-1113-9.

[7] V. Becattini et al. "Pilot-scale demonstration of advanced adiabatic compressed air energy storage, Part 2: Tests with combined sensible/latent thermal-energy storage". In: *Journal of Energy Storage* 17 (2018), pp. 140–152. DOI: 10.1016/j.est.2018.02.003.

[8] Felix Birkelbach. *Non-Parametric Kinetic Modelling of Gas-Solid Reactions for Thermocemical Energy Storage*. Dissertation: TU Wien, 2020.

[9] Alejandra Borunda. *What a 100-Degree Day in Siberia Really Means*. National Geographic, Science, 2020. URL: https://www.nationalgeographic.com/science.

[10] Robert W. Carling. "Heat capacities of NaNO3 and KNO3 from 350 to 800 K". In: *Thermochimica Acta* 60.3 (1983), pp. 265–275. ISSN: 00406031. DOI: 10.1016/0040-6031(83)80248-2.

[11] J. C. Choi and Kim S.D. "Heat-Transfer Characteristics of a Latent Heat Thermal Energy Storage System Using MgCl2.6H2O". In: *Energy* 17 (1992), pp. 1153–1164. ISSN: 03605442.

[12] K. Couvreur et al. "Experimental behavior of a 100 kWhth fin-tube latent heat storage using eutectic KNO3-NaNO3 as PCM". In: *Advances in Thermal Energy*

Storage. Ed. by Universitat de Lleida. Edicions de la Universitat de Lleida, 2019, pp. 451–460. ISBN: 978-84-9144-155-7.

[13] Kenny Couvreur et al. "Hot water storage for increased electricity production with organic Rankine cycle from intermittent residual heat sources in the steel industry". In: *Energy* 200 (2020), p. 117501. ISSN: 03605442. DOI: 10.1016/j.energy.2020.117501.

[14] F. Crotogino, K. U. Mohmeyer, and R. Scharf. "Huntorf CAES: More than 20 years of successful operation". In: *SMRI Spring Meeting* 50 (2001), pp. 351–362. URL: www.scopus.com.

[15] F. Crotogino and P. Quast. "COMPRESSED-AIR STORAGE CAVERNS AT HUNTORF". In: *Subsurface space*. Ed. by S. Magnus Bergman. Oxford and New York: Pergamon Press, 1981, pp. 593–600. ISBN: 9781483284217. DOI: 10.1016/B978-1-4832-8421-7.50085-5.

[16] John Daly et al. "CAES: Reduced to Practice". In: *ASME turbo expo*. [New York]: American Society of Mechanical Engineers, 2001. ISBN: 978-0-7918-7852-1. DOI: 10.1115/2001-GT-0397.

[17] DNV-GL. *Energy Transition Outlook 2019: A global and regional forecast to 2050*. Oslo: Det Norske Veritas & Germanischer Lloyd, 2019. URL: https://eto.dnvgl.com/2019.

[18] U. S. Department of Energy. *DOE Global Energy Storage Database*. Ed. by Office of Electricity &. Energy Reliability U.S. Department of Energy. 2019. URL: https://www.sandia.gov/ess-ssl/global-energy-storage-database-home/ (visited on 06/04/2020).

[19] M. M. Farid and A. Kanzawa. "Thermal Performance of a Heat Storage Module Using PCM's with Different Melting Temperatures: Mathematical Modelling". In: *ASME Journal of Solar Energy Engineering* 111 (1989), pp. 152–207.

[20] Amy S. Fleischer. *Thermal Energy Storage Using Phase Change Materials: Fundamentals and Applications*. SpringerBriefs in Applied Sciences and Technolog, 2015. ISBN: 9783319209227. URL: http://dx.doi.org/10.1007/978-3-319-20922-7.

[21] Jaume Gasia et al. "Experimental evaluation of the use of fins and metal wool as heat transfer enhancement techniques in a latent heat thermal energy storage system". In: *Energy Conversion and Management* 184 (2019), pp. 530–538. ISSN: 01968904. DOI: 10.1016/j.enconman.2019.01.085.

[22] Jaume Gasia et al. "Influence of the storage period between charge and discharge in a latent heat thermal energy storage system working under partial load operating conditions". In: *Applied Energy* 235 (2019), pp. 1389–1399. ISSN: 03062619. DOI: 10.1016/j.apenergy.2018.11.041.

[23] Jaume Gasia et al. "Use of partial load operating conditions for latent thermal energy storage management". In: *Applied Energy* 216 (2018), pp. 234–242. ISSN: 03062619. DOI: 10.1016/j.apenergy.2018.02.061.

[24] L. Geissbühler et al. “Pilot-scale demonstration of advanced adiabatic compressed air energy storage, Part 1: Plant description and tests with sensible thermal-energy storage”. In: *Journal of Energy Storage* 17 (2018), pp. 129–139. DOI: 10.1016/j.est.2018.02.004.

[25] Dominic Groulx. “The rate problem in solid-liquid phase change heat transfer: Efforts and questions towards heat exchanger design rules”. In: *16th International Heat Transfer Conference (IHTC-16)*. Ed. by International Heat Transfer Conferences. 2018.

[26] C. Guo and Zhang W. “Numerical Simulation and Parametric Study on New Type of High Temperature Latent Heat Thermal Energy Storage System”. In: *Energy Conversion and Management* 49 (2008), pp. 919–927. ISSN: 01968904.

[27] IEA. *Energy Storage*. Paris: IEA Publications, 2020. URL: https://www.iea.org/reports/energy-storage.

[28] IEA. *World Energy Outlook 2019*. Paris: IEA Publications, 2019. ISBN: 9264973001. URL: https://www.iea.org/reports/world-energy-outlook-2019.

[29] IPCC. *Global warming of 1.5°C: An IPCC Special Report on the impacts of global warming of 1.5°C above pre-industrial levels and related global greenhouse gas emission pathways*. Geneva: Intergovernmental Panel on Climate Change, 2018. URL: https://www.ipcc.ch/sr15.

[30] IRENA. *Electricity Storage and Renewables: Costs and Markets to 2030*. International Renewable Energy Agency, 2017. ISBN: 978-92-9260-038-9. URL: https://www.irena.org/publications.

[31] IRENA. *Global Renewables Outlook: Energy transformation 2050*. Abu Dhabi: International Renewable Energy Agency, 2020. ISBN: 978-92-9260-238-3. URL: https://www.irena.org/publications.

[32] IRENA. *Renewable Energy Statistics 2020*. Abu Dhabi: International Renewable Energy Agency, 2020. URL: https://www.irena.org/publications.

[33] IRENA. *Renewables and Electricity Storage: A Technology Roadmap for REmap 2030*. International Renewable Energy Agency, 2015. ISBN: 978-92-95111-65-3. URL: https://www.irena.org/publications.

[34] S. Jegadheeswaran and Sanjay D. Pohekar. “Performance enhancement in latent heat thermal storage system: A review”. In: *Renewable and Sustainable Energy Reviews* 13.9 (2009), pp. 2225–2244. ISSN: 13640321. DOI: 10.1016/j.rser.2009.06.024.

[35] M. Johnson et al. “High Temperature Latent Heat Thermal Energy Storage Integration in a Co-gen Plant”. In: *Energy Procedia* 73 (2015), pp. 281–288. ISSN: 18766102. DOI: 10.1016/j.egypro.2015.07.689.

[36] Maike Johnson, Bernd Hachmann, and Andreas J. Dengel. “Design and integration of high temperature latent heat thermal energy storage for high power levels”. In:

International Mechanical Engineering Congress and Exposition IMECE2018. Ed. by ASME. ASME, 2018, pp. 1–8. ISBN: 978-0-7918-5208-8.

[37] Maike Johnson et al. "Design of high temperature thermal energy storage for high power levels". In: *Sustainable Cities and Society* 35 (2017), pp. 758–763. ISSN: 22106707. DOI: 10.1016/j.scs.2017.09.007.

[38] Maike Johnson et al. "Experimental analysis of the performance of optimized fin structures in a latent heat energy storage test rig". In: *AIP Conference Proceedings*, p. 080013. DOI: 10.1063/1.4984434.

[39] Maike Johnson et al. "Large-scale high temperature and power latent heat storage unit development". In: *AIP Conference Proceedings*, p. 200023. DOI: 10.1063/1.5117738.

[40] T. Jriri et al. "Thermodynamic study of the condensed phases of NaNO3, KNO3 and CsNO3 and their transitions". In: *Thermochimica Acta* 266 (1995), pp. 147–161. ISSN: 00406031. DOI: 10.1016/0040-6031(95)02337-2.

[41] K. C. Kavvadias, A. P. Tosios, and Z. B. Maroulis. "Design of a combined heating, cooling and power system: Sizing, operation strategy selection and parametric analysis". In: *Energy Conversion and Management* 51.4 (2010), pp. 833–845. ISSN: 01968904. DOI: 10.1016/j.enconman.2009.11.019.

[42] S. Krishnan, J. Y. Murthy, and S. V. Garimella. "A Two-Temperature Model for Solid-Liquid Phase Change in Metal Foams". In: *Journal of Heat Transfer* 127.9 (2005), pp. 995–1004. ISSN: 0022-1481. DOI: 10.1115/1.2010494.

[43] M. Lacroix. "Study of the Heat Transfer Behaviour of a Latent Heat Thermal Energy Storage Unit with a Finned Tube". In: *International Journal of Heat and Mass Transfer* 36 (1993), pp. 2083–2092. ISSN: 00179310.

[44] Osama Mesalhy et al. "Numerical study for enhancing the thermal conductivity of phase change material (PCM) storage using high thermal conductivity porous matrix". In: *Energy Conversion and Management* 46.6 (2005), pp. 847–867. ISSN: 01968904. DOI: 10.1016/j.enconman.2004.06.010.

[45] H. Michels and R. Pitz-Paal. "Cascaded Latent Heat Storage for Parabolic Trough Solar Power Plants". In: *Solar Energy* 81 (2007), pp. 829–837.

[46] M. Nakhamkin et al. "AEC 110 MW CAES Plant: Status of Project". In: *Journal of Engineering for Gas Turbines and Power* 114.4 (1992), pp. 695–700. ISSN: 0742-4795. DOI: 10.1115/1.2906644.

[47] Hassan Nazir et al. "Recent developments in phase change materials for energy storage applications: A review". In: *International Journal of Heat and Mass Transfer* 129 (2019), pp. 491–523. DOI: 10.1016/j.ijheatmasstransfer.2018.09.126.

[48] Ugo Pelay et al. "Thermal energy storage systems for concentrated solar power plants". In: *Renewable and Sustainable Energy Reviews* 79 (2017), pp. 82–100. ISSN: 13640321. DOI: 10.1016/j.rser.2017.03.139.

[49] Alberto Pizzolato et al. “Design of effective fins for fast PCM melting and solidification in shell-and-tube latent heat thermal energy storage through topology optimization”. In: *Applied Energy* 208 (2017), pp. 210–227. ISSN: 03062619. DOI: 10.1016/j.apenergy.2017.10.050.

[50] A. Prötsch. *Auslegung und Inbetriebnahme einer Latentwärmespeicherversuchsanlage*. TU Wien, 2012.

[51] Ahmet Sarı and Ali Karaipekli. “Thermal conductivity and latent heat thermal energy storage characteristics of paraffin/expanded graphite composite as phase change material”. In: *Applied Thermal Engineering* 27.8-9 (2007), pp. 1271–1277. ISSN: 13594311. DOI: 10.1016/j.applthermaleng.2006.11.004.

[52] Georg Scharinger-Urschitz, Heimo Walter, and Markus Haider. “Heat Transfer in Latent High-Temperature Thermal Energy Storage Systems—Experimental Investigation”. In: *Energies* 12.7 (2019), p. 1264. ISSN: 1996-1073. DOI: 10.3390/en12071264.

[53] Georg Scharinger-Urschitz et al. “Partial cycle operation of latent heat storage with finned tubes”. In: *Applied Energy* 280 (2020), p. 115893. ISSN: 0306-2619. DOI: https://doi.org/10.1016/j.apenergy.2020.115893. URL: http://www.sciencedirect.com/science/article/pii/S0306261920313611.

[54] A. Sciacovelli, F. Gagliardi, and V. Verda. “Maximization of performance of a PCM latent heat storage system with innovative fins”. In: *Applied Energy* 137 (2015), pp. 707–715. ISSN: 03062619. DOI: 10.1016/j.apenergy.2014.07.015.

[55] Atul Sharma et al. “Review on thermal energy storage with phase change materials and applications”. In: *Renewable and Sustainable Energy Reviews* 13.2 (2009), pp. 318–345. ISSN: 13640321. DOI: 10.1016/j.rser.2007.10.005.

[56] UNFCCC. *Adoption of the Paris Agreement*. Paris: United Nations Framework Convention on Climate Change, 21st Conference of the Parties, 2015.

[57] Georg Urschitz, Heimo Walter, and Michael Hameter. “Laboratory Test Rig of a LHTES (Latent Heat Thermal Energy Storage): Construction and First Experimental Results”. In: *Journal of Energy and Power Engineering* 8 (2014), pp. 1838–1847.

[58] B. Vanslambrouck et al. “Constant Power Production with an Organic Rankine Cycle from a Fluctuating Waste Heat Source by Using Thermal Storage”. In: *8th Heat Powered Cycles Conference 2018*. Vol. 493-501.

[59] R. Velraj et al. “Heat Transfer Enhancement in a Latent Heat Storage System; Paper presented at the ISES Solar World Congress, Taejon, South Korea, 24–29 August 1997.1”. In: *Solar Energy* 65.3 (1999), pp. 171–180. DOI: 10.1016/S0038-092X(98)00128-5.

[60] Heimo Walter, Anton Beck, and Michael Hameter. “Influence of the Fin Design on the Melting and Solidification Process of NaNO3 in a Thermal Energy Storage

System". In: *Journal of Energy and Power Engineering* 9.11 (2015). DOI: 10.17265/1934-8975/2015.11.001.

[61] J. Wang, Y. Ouyang, and G. Chen. "Experimental Study on Charging Processes of a Cylindrical Heat Storage Capsule Employing Multiple-Phase-Chang Materials". In: *International Journal of Energy Research* 25 (2001), pp. 439–447.

[62] Yin Huibin et al. "Experimental research on heat transfer mechanism of heat sink with composite phase change materials". In: *Energy Conversion and Management* 49.6 (2008), pp. 1740–1746. ISSN: 01968904. URL: http://inis.iaea.org/search/search.aspx?orig_q=RN:40016363.

[63] H. L. Zhang et al. "Concentrated solar power plants: Review and design methodology". In: *Renewable and Sustainable Energy Reviews* 22 (2013), pp. 466–481. ISSN: 13640321. DOI: 10.1016/j.rser.2013.01.032.

[64] H. L. Zhang et al. "Latent heat storage with tubular-encapsulated phase change materials (PCMs)". In: *Energy* 76 (2014), pp. 66–72. ISSN: 03605442. DOI: 10.1016/j.energy.2014.03.067.

[65] Hanfei Zhang et al. "Microencapsulation of molten salt in stable silica shell via a water-limited sol-gel process for high temperature thermal energy storage". In: *Applied Thermal Engineering* 136 (2018), pp. 268–274. ISSN: 13594311. DOI: 10.1016/j.applthermaleng.2018.02.050.

[66] Huili Zhang et al. "Thermal energy storage: Recent developments and practical aspects". In: *Progress in Energy and Combustion Science* 53 (2016), pp. 1–40. ISSN: 03601285. DOI: 10.1016/j.pecs.2015.10.003.

[67] Y. Zhang and A. Faghri. "A Heat Transfer Enhancement in Latent Heat Thermal Energy Storage System by Using an External Radial Finned Tube". In: *Journal of Enhanced Heat Transfer* 36 (1996), pp. 119–127.

[68] Gabriel Zsembinszki et al. "Evaluation of the State of Charge of a Solid/Liquid Phase Change Material in a Thermal Energy Storage Tank". In: *Energies* 13.6 (2020), p. 1425. ISSN: 1996-1073. DOI: 10.3390/en13061425.

List of Figures

List of Tables

A. Appendix

In Appendix A.1 additional temperature trends of all partial cycle experiments which were carried out and used to calculate the results in Chapter 5 are shown. Every trend includes the HTF-temperatures, the PCM-temperatures as well as the *SOC*.

The MATLAB-function which was developed for the calculation of the thermo-physical properties of sodium nitrate is provided in Appendix A.2. This function is valid for temperatures between 0 and 400 °C and at ambient pressure. The function can be used to calculate the specific heat capacity in $\mathrm{kJ\,kg^{-1}\,K^{-1}}$ (syntax: *nano3.c(T)*, T...temperature in °C) and the specific enthalpy in $\mathrm{kJ\,kg^{-1}}$ (syntax: *nano3.h(T)*, T...temperature in °C). The specific enthalpy is set to 0 $\mathrm{kJ\,kg^{-1}}$ at 0 °C. Both functions are based on experimental data from Jriri et al. [40] and Carling et al. [10].

A.1. Temperature Trends

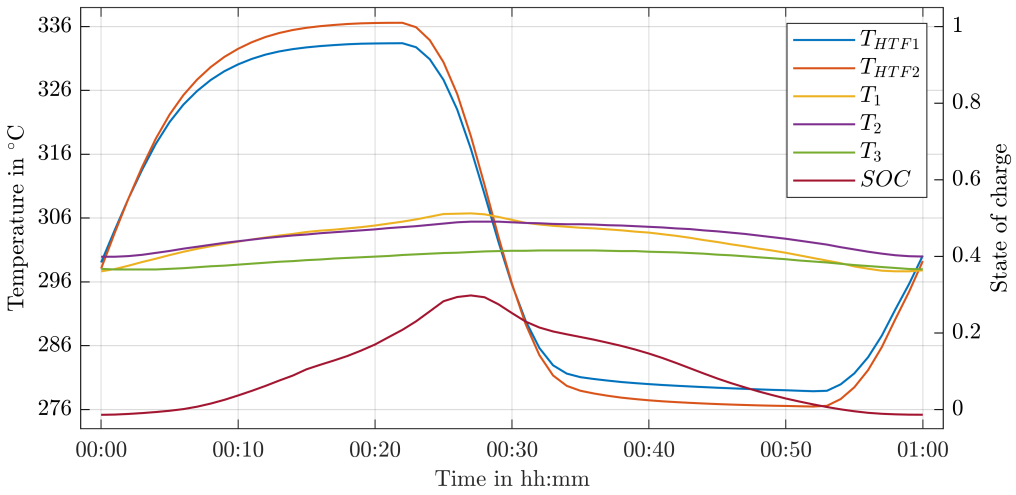

Figure A.1.: *Temperature trends for SOC 0.00-0.25 cycle*

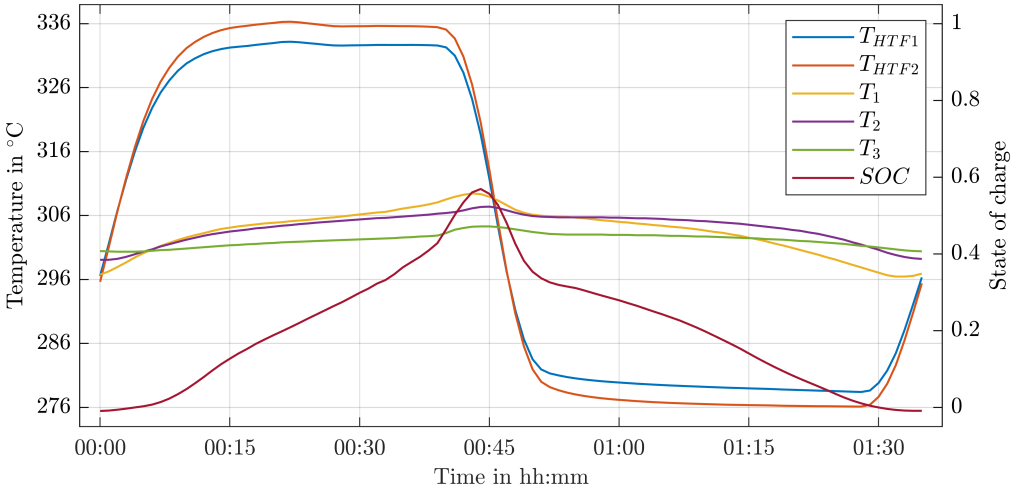

Figure A.2.: *Temperature trends for SOC 0.00-0.50 cycle*

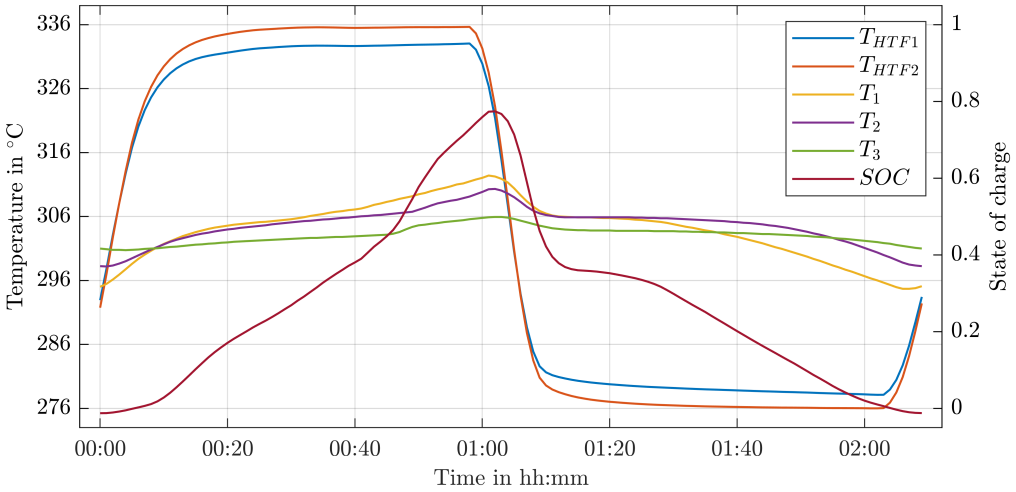

Figure A.3.: *Temperature trends for SOC 0.00-0.75 cycle*

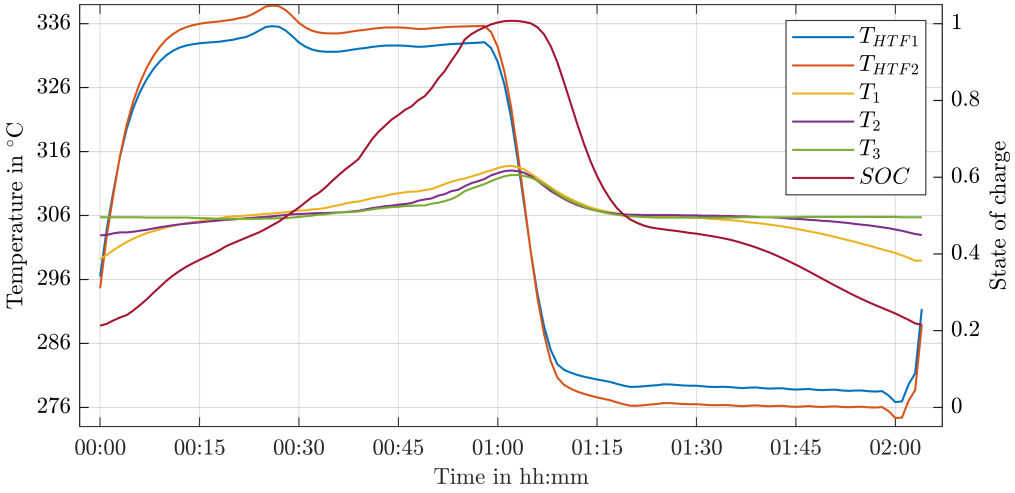

Figure A.4.: *Temperature trends for SOC 0.25-1.00 cycle*

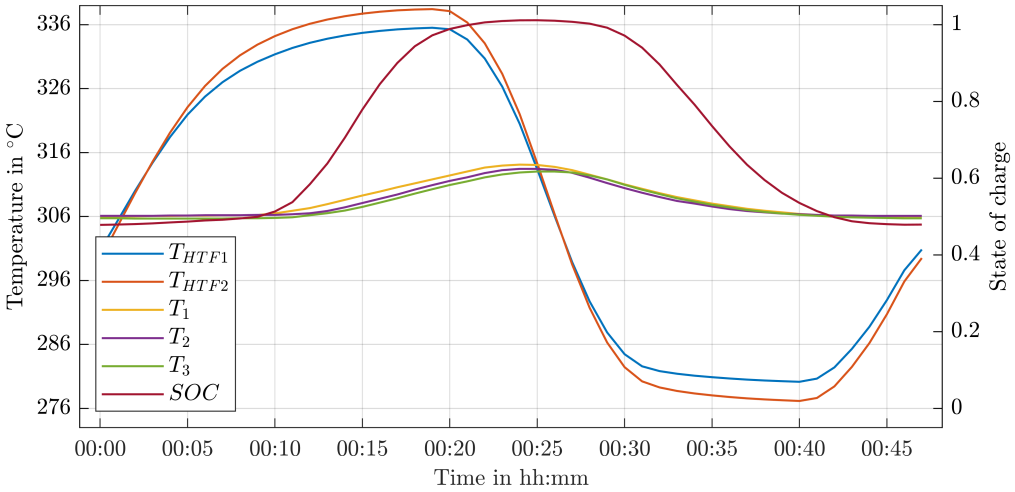

Figure A.5.: *Temperature trends for SOC 0.50-1.00 cycle*

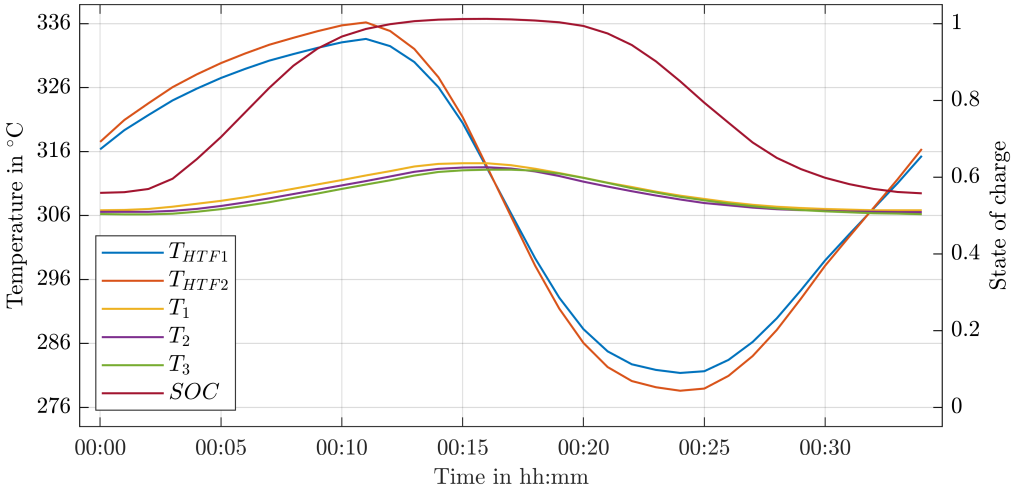

Figure A.6.: *Temperature trends for SOC 0.75-1.00 cycle*

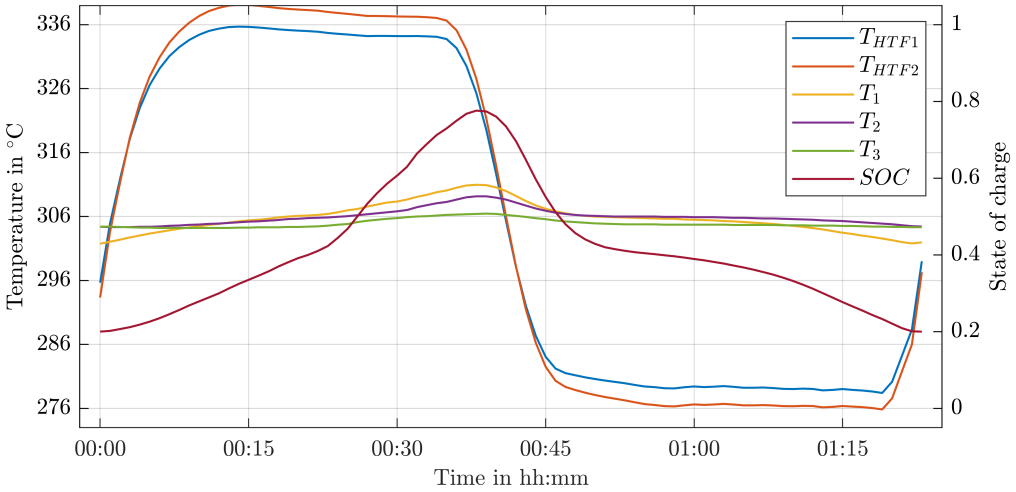

Figure A.7.: *Temperature trends for SOC 0.25-0.75 cycle*

A.2. Matlab Functions

```
classdef nano3
    %Calculate properties of pure sodium nitrate (NaNO3)
    %
    %nano3.c(T) returns the specific heat capacity in kJ/kgK
    %at the temperature given by T (T in centigrade)
    %nano3.h(T) returns the specific enthalpy in kJ/kg
    %at the temperature given by T (T in centigrade)
    %
    %c(T) in kJ/kgK
    %h(T) in kJ/kg, h(0)=0 Enthalpy is set to 0 at T=0
    %Valid temperature range from 100 to 400 centigrade
    %
    %Based on data from T. Jriri. Thermodynamic study of the
    %condensed phases of NaNO3, KNO3 and CsNO3 and their
    %transitions, 1995. & R. Carling. Heat capacities of
    %NaNO3 and KNO3 from 350 to 800K, 1982

    %(c) Georg Scharinger-Urschitz & Paul Schwarzmayr
    %Institute for Energy Systems and Thermodynamics, TU Wien

    properties (Constant)
        T_s = 300;  %Solidification temperature
        T_l = 312;  %liquifidation temperature

        Tlim = [0 T_s T_l 400]; %limits for the validity ranges
            of cFun and hFun
        %Functions for the specific heat capacity
        cFun = { @(T) 0.003214 * T+0.9262,...
                 @(T) polyval([0.0216147 -0.51873 3.11031
                    0.003214 1.8904],(T-300)),...
                 @(T) 1.65};
        %Functions for the specific enthalpy
        hFun = { @(T) polyval([0.001607 0.9262 0],T),...
                 @(T) polyval([0.00432294 -0.1296825 1.03667
                    0.001607 1.8904 0],(T-300)),...
                 @(T) polyval([1.65 0],(T-312))}
    end

    methods (Static)    %Properties of NaNO3
        function c = c(T)   %Specific heat capacity in kJ/kgK
            %Transpose T, if T is a row vector
```

```
39              if size(T,2)>1
40                  T=T.';
41              end
42              %Calculate c(T)
43              c = zeros(size(T,1),1);
44              for i = 1:numel(nano3.cpFun)
45                  idx = nano3.Tlim(i)<=T & T<=nano3.Tlim(i+1);
46                  c(idx) = nano3.cpFun{i}(T(idx));
47              end
48              %If any input value is out of validity range,
                    awarning is displayed
49              idx = 100 > T | T > nano3.Tlim(4);
50              if any(idx)
51                  warning('Some values are out of range! Only
                        values from 100 to 400  C  are valid');
52              end
53          end
54
55          function h = h(T)   %Specific enthalpy in kJ/kg
56              %Transpose T, if T is a row vector
57              if size(T,2)>1
58                  T=T.';
59              end
60              %Calculate h(T)
61              h = zeros(size(T,1),1);
62              for i = 1:numel(nano3.hFun)
63                  idx = nano3.Tlim(i) < T & T <= nano3.Tlim(i+1);
64                  h(idx) = h(idx) + nano3.hFun{i}(T(idx));
65                  idx = T > nano3.Tlim(i+1);
66                  h(idx)=h(idx)+nano3.hFun{i}(nano3.Tlim(i+1));
67              end
68              %If any input value is out of validity range,
                    awarning is displayed
69              idx = 100 > T | T > nano3.Tlim(4);
70              if any(idx)
71                  warning('Some values are out of range! Only
                        values from 100 to 400  C  are valid');
72              end
73          end
74      end
75  end
```